A99-16309

AIAA 99-0416
Numerical Simulation of Transient Hypersonic Flow with Real Gas Effects

Yanbao Ma and Xiaolin Zhong
University of California, Los Angeles
Los Angeles, CA

37th Aerospace Sciences Meeting & Exhibit
January 11–14, 1999 / Reno, NV

Numerical Simulation of Transient Hypersonic Flow with Real Gas Effects

Yanbao Ma*and Xiaolin Zhong†

University of California, Los Angeles, CA 90095

1 Abstract

A high-order upwind finite difference shock fitting scheme combined with additive semi-implicit Runge-Kutta (SIRK) methods is used in numerical simulation of transient hypersonic nonequilibrium flow. Partially dissociated nitrogen passing over cylinders is computed as a test case compared with experimental results as well as other published computational results. The heat flux at the stagnation point is computed and compared with that obtained from boundary layer solutions. The ability of the computations presented in this paper to accurately capture the shock shapes ,the standoff distances and heat flux at stagnation point, demonstrates the capability of the code to sufficiently model flows in thermochemical nonequilibrium. The code is also extended and tested to simulate unsteady nonequilibrium flow to study the additional real gas effects on flow properties such as receptivity, stability and heat transfer.

2 Introduction

The design of future space transportation vehicles, especially the development of new cheaper reusable launch systems, cause great interest to investigate hypersonic nonequilibrium flow. The laminar-turbulent transition in thermally and chemically nonequilibrium boundary layer at hypersonic speeds significantly affects the vehicle performance and surface heating. Therefore, the accurate prediction of boundary layer transion is a critical part for aerodynamic design of vehicle and thermal protection system. When an aerospace vehicle travels through the atmosphere at hypersonic speed, the Mach number is high and the bow shock wave is strong. The shock converts the kinetic energy of the stream to internal energy, raising the temperature to a value where real gas effects are required to be considered. The phrase "real gas" used in this paper is in the sense of aerodynamics where it typifies the high-temperature effects, involving the the sense of classical physical chemistry where it has been used for a gas in which intermolecular forces are important due to high pressures and/or low temperatures. Such real gas effects not only mean the departure from perfect gas even if in thermodynamical equilibrium, but also introduce two time scales if the rates of dissociation and excitation of vibration are finite, which depends on gas and flow conditions. The departure from perfect gas depends on temperature as well as pressure. For example, at a pressure of 1 atm, vibrational excitation begins at about $800°K$. When temperatures exceed about $2500°K$, oxygen molecules begin to dissociate while nitrogen begins at about $4000°K$. At about $9000°K$ or higher, there is significant ionization taking place [1]. In various flow situations, nonequilibrium of rotational, vibrational, electronic, and chemical modes can be observed. The approach to equilibrium of these various modes is governed by kinetic equations that are first-order in their time derivatives [2]. Examination of these equations reveals a time scale of relaxation time for the equilibration of the mode under consideration. The rotational modes require only a few molecular collisions to equilibrate, while vibrational equilibration is a process with relaxation time between the very short time for rotational equilibration and the longer time for ionization and chemical equilibration. At extremely high temperature, all processes are very closely coupled. Such high temperatures are possible near the nose of a hypersonically traveling vehicle depending upon its velocity and altitude. The dissociation rate falls rapidly with decrease of the temperature and therefore with shock slope. Thus the region affected by the chemical relaxtion is limited to the vicinity of the stagnation point. Immediately behind the bow shock wave in the stagnation region of a vehicle, the vibrational temperature may overshoot the equilibrium post-shock temperature. When the population of excited electronic states is governed by the vibrational temperature due to the dramatic increase of super-equilibrium molecules, thermal radiation as photons is significant as the excited electronic states decay to the ground state. Many phontons are absorbed by the body surface, which leads to a significant increase

*Graduate Student Researcher, Department of Mechanical and Aerospace Engineering

†Associate Professor, Department of Mechanical and Aerospace Engineering, Member AIAA.

in the heat transfer rate due to nonequilibrium. For many flight conditions, dissociated atoms recombine near the wall. The effect of the body surface on the recombination rates near the wall is described by wall catalycity. The catalycity can change the composition of the flow and increase the heat transfer. Theoretically, the catalycity ranges from a fully catalytic condition to a noncatalytic one. For a noncatalytic wall, no recombination occurs at the wall and the resulting heat transfer can be much less. However, a fully catalytic wall will cause recombination to occur instantaneously and increase heat transfer due to the heat released from exothermic recombination reactions. A finite-catalytic wall is one which produces a situation between these two extremes. The vibrational-dissociational interaction, nonequilibrium thermal radiation, wall catalycity are primary uncertainties in modeling hypersonic flows. All these issues have been extensively studied. Many models have been presented to describe these processes [3-5]. An overview of these fields spanning a period of nearly four decade can be found in [6-11].

The accurate simulation of transient flow is important for the prediction of laminar-turbulent boundary layer transition(Fig.1). The fundamental causes of boundary layer transition are identified in stability analyses. In general, the transition is a result of nonlinear response of the laminar boundary layers to forcing disturbances [12-15]. The forcing disturbances [16] can originate from many difference sources, including freestream disturbances. In an environment with small initial disturbances, the paths to transition consist of three stages: 1) receptivity, 2) linear eigenmode growth or transient growth, and 3) nonlinear breakdown to turbulence. The first stage is the receptivity process [17], which converts the environmental disturbances into instability, Tollmien-Schlichting (T-S), waves in the boundary layers. The second stage is the linear eigenmode growth of boundary-layer instability waves obtained as the eigen-solutions of the homogeneous linearized disturbance equations. The relevant instability waves developed in hypersonic boundary layers are the T-S wave and inviscid waves of higher (Mack) modes discovered by Mack [18,19], the Görtler instability [20] over concave surfaces, and the three-dimensional cross flow instability [21]. The third stage is the breakdown of linear instability waves and transition to turbulence after the growth of linear instability waves reach certain magnitudes. The receptivity mechanism provides important initial conditions of amplitude, frequency, and phase for the instability waves in the boundary layers [22-24].

To date, linear stability theory (LST) is still the main approach for prediction of transition. The results of LST are very sensitive to the accuracy of the base flows. In a hypersonic flow over a blunt body, the thermal and chemical nonequilibrium significantly change the flow field. In addition, real gas effects may change the growth rate of instability modes and add new instability mode. The stability analyses with the consideration of real gas effects can be found in the works of Malik , Anderson, [25,26], Stuchert and Reed [27], Hudson, Choknai and Candler [28,29], Chang, Vinh and Malik [30]. Two experimental results in this field can be found in the works of Kendall [31,32], Adam and Hornung [33].

In stability analyses, an accurate computation of the mean and transient hypersonic flow is critical for many hypersonic applications. One reason is due to the fact that many shock boundary layer interactions have been found to be inherently unsteady, and the unsteadiness has strong effects on the aerodynamic parameters of the flows. Even within perfect gas regime, hypersonic flow associated with such phenomena are inherently transient three-dimensional flows containing a wide range of time and length scales. The real gas effects add more time and length scales related to finite rates of dissociation and excitation of vibration. The numerical simulation of such transient flows require high-order accurate CFD methods in order to capture all of these time and length scales of flow. Standard shock-capturing CFD methods developed for steady or slightly unsteady flow computation are not appropriate for transient applications because their accuracy level is not high enough.

The purpose of this paper is to apply a high-order upwind finite difference shock fitting scheme combined with additive semi-implicit Runge-Kutta (SIRK) methods developed by Zhong [34] to simulate transient hypersonic boundary layer flow with thermal and chemical nonequilibrium in continuum regime. High-order of both spatial discretization and temporal integration is necessary. Fifth-order upwind finite difference scheme is used to discretize convective terms while sixth-order central difference scheme is used for viscous terms. For simulation of viscous hypersonic flows over blunt body, flow properties such as temperature, species mass fraction, and density may dramatically change in the shock layer immediately behind the shock and in boundary layer near the body due to chemical reaction and wall conditions. Grids for computation are strongly stretched in both of the two regions in order to cluster more grids points in them. Fifth-order polynomial interpolation directly to the stretched physical grid without using the coordinate transformation is applied for the purpose of numerical stability consideration [35]. The spatial discretization of the governing equations leads to a system of first-order ordinary differential equations. Third-order Semi-implicit Runge-Kutta scheme [34] is used for temporal integra-

tion, which splits the governing equations into non-stiff terms resulting from spatial discretization of the flux terms that can be computed explicitly and stiff terms containing the thermal-chemical source terms that need to be computed implicitly.

To validate this numerical method and computational code, steady hypersonic flow past cylinders based on Hornung's [36]experimental data is computed. The results are compared with experimental and Furumoto's [37] computational results. Heat flux at the stagnation point is compared with classical results of Fay and Riddell [38]. Vibrationally relaxing flow of N_2 past an infinite cylinder is studied and compared with the results of Giordano [39]. The additional real gas effects on flow properties such as receptivity, stability and heat transfer are studied. The numerical results show that the real gas effects significantly change flow field including the standoff distance of bow shock over the front part of blunt body and other flow properties.

3 Physical Model And Governing Equations

Physical models used for the numerical simulations of nonequilibrium hypersonic flows must capture the complex thermophysical phenomena that characterize these flows. Detailed discussions of the relevant flow physics can be found in works by Vincenti and Kruger [40] and Clarke and McChensey [41] There are many different ways to formulate the governing equations for nonequilibrium flow, depending on what approximations are made in the modeling process. In the context of continuum based numerical simulations, some of the more well known are outlined in works by Park [42], Lee [43], Gupta, *et al.* [44], and Häuser, *et al.* [45] The work presented in the remainder of this paper uses nonequilibrium models based primarily on those of Park and Häuser [42,45]. Governing equations are formulated for a two-temperature model with five species (non-ionizing) finite rate air chemistry with assumption that the rate of rotational relaxation approachs infinity, and the rotational energy is fully excited (*i.e.*, rotatioal temperature equals translational temperature). In the following sections, sums are taken over indices ranging from 1 to either NS or nd. NS is the total number of species being considered, while nd is the number of diatomic species being considered.

3.1 Equations of motion

In conservative form, the multicomponent Navier-Stokes Equations, along with vibrational energy equations, are:

$$\frac{\partial \rho_i}{\partial t} + \frac{\partial}{\partial x}(\rho_i u + j_{ix}) + \frac{\partial}{\partial y}(\rho_i v + j_{iy}) + \frac{\partial}{\partial z}(\rho_i w + j_{iz}) = w_i \quad (1)$$

$$\frac{\partial (\rho u)}{\partial t} + \frac{\partial}{\partial x}(\rho u^2 + p - \tau_{xx}) + \frac{\partial}{\partial y}(\rho uv - \tau_{xy}) + \frac{\partial}{\partial z}(\rho uw - \tau_{xz}) = 0 \quad (2)$$

$$\frac{\partial (\rho v)}{\partial t} + \frac{\partial}{\partial x}(\rho uv - \tau_{xy}) + \frac{\partial}{\partial y}(\rho v^2 + p - \tau_{yy}) + \frac{\partial}{\partial z}(\rho vw - \tau_{yz}) = 0 \quad (3)$$

$$\frac{\partial (\rho w)}{\partial t} + \frac{\partial}{\partial x}(\rho uw - \tau_{xz}) + \frac{\partial}{\partial y}(\rho vw - \tau_{yz}) + \frac{\partial}{\partial z}(\rho w^2 + p - \tau_{zz}) = 0 \quad (4)$$

$$\frac{\partial E_v}{\partial t} + \frac{\partial}{\partial x}(uE_v + q_{vx}) + \frac{\partial}{\partial y}(vE_v + q_{vy}) + \frac{\partial}{\partial z}(wE_v + q_{vz}) = w_v \quad (5)$$

$$\frac{\partial E}{\partial t} + \frac{\partial}{\partial x}[u(E+p) - u\tau_{xx} - v\tau_{xy} - w\tau_{xz} + q_x] + \frac{\partial}{\partial y}[v(E+p) - u\tau_{xy} - v\tau_{yy} - w\tau_{yz} + q_y] + \frac{\partial}{\partial z}[w(E+p) - u\tau_{xz} - v\tau_{yz} - w\tau_{zz} + q_z] = 0 \quad (6)$$

where E_v and E are the vibrational and total energies per unit volume, the w_i's are the chemical source terms for species i, and w_v is the source terms for the vibrational mode. These equations, as presented, do not form a mathematically closed set. In order to close this set of equations, thermodynamic equations of state and constitutive relations for the viscous fluxes are required.

3.2 Equations of state

Closure of the governing equations requires thermodynamic state equations. The system is taken to be a mixture of thermally perfect gases with the following equation of state:

$$p = \rho R T_t \tag{7}$$

where p and ρ are the bulk pressure and density, respectively, T_t is the translational temperature, and R is the mass averaged gas constant, defined as:

$$R = \sum_{i=1}^{NS} \frac{\rho_i}{\rho} R_i \tag{8}$$

where R_i is the species specific gas constant.

The internal vibrational energy mode is modeled by a separate temperature, T_v [46–48]. The internal energy equation for a diatomic species is then:

$$e_i = \frac{5}{2} R_i T_t + e_{vi} + h_i^\circ \tag{9}$$

$$e_{vi} = R_i \frac{\theta_{vi}}{e^{\theta_{vi}/T_v} - 1} \tag{10}$$

Correspondingly, the equation for a monatomic species is:

$$e_i = \frac{3}{2} R_i T_t + h_i^\circ \tag{11}$$

In the above equations, θ_{vi} is the characteristic vibrational temperature of species i and h_i° is the species heat of formation. These values are given in Table 1.

The vibrational and total energies per unit volume are given by:

$$E_v = \sum_{i=1}^{nd} \rho_i e_{vi} \tag{12}$$

$$E = \sum_{i=1}^{NS} \rho_i e_i + \rho \frac{u^2 + v^2}{2} \tag{13}$$

3.3 Constitutive relations

The viscous terms in the governing equations (viscous stresses, diffusive fluxes, and heat fluxes) require constitutive relations to relate these viscous terms to the flow and thermodynamic variables. The viscous stresses are modeled using the Navier-Stokes equations:

$$\tau_{ij} = -\mu \left(\frac{\partial u_i}{\partial x_j} + \frac{\partial u_j}{\partial x_i} \right) + 2\mu/3 \frac{\partial u_k}{\partial x_k} \delta_{ij} \tag{14}$$

For chemically reacting flow, species mass diffusion fluxes are given by full multicomponent diffusion models where the flux of species i is dependent upon its own concentration gradient, and the gradients of all the other species [49–51]. Such a multicomponent model can be computationally prohibitive for numerical simulations. Therefore, a common approximate model used is to assume each species follows Fick's Law of diffusion for a binary gas mixture. Thus, each species is treated as diffusing into the remaining bulk as if it were a binary mixture of the species in question and everything else. Using this model, the mass diffusion fluxes for species i are given by:

$$j_{ix_k} = -\rho D_i \frac{\partial (\rho_i/\rho)}{\partial x_k} \tag{15}$$

The effects of diffusion due to thermal and pressure gradients are typically small and can be neglected for simplicity [52].

Heat diffusion is modeled using Fourier's Law for heat conduction:

$$q_{x_k} = -(\kappa_t + \kappa_r) \frac{\partial T_t}{\partial x_k} - \kappa_v \frac{\partial T_v}{\partial x_k} + \sum_{i=1}^{NS} j_{ix_k} h_i \tag{16}$$

with the total enthalpy, h_i, given by:

$$h_i = e_i + R_i T_t \tag{17}$$

3.4 Transport coefficients

The transport coefficients need to be modeled for a gas mixture. Individual species viscosities (μ_i) are calculated using a curve fit model presented by Moss [53]:

$$\mu_i = \exp\left[(A_i \ln T_t + B_i) \ln T_t + C_i \right] \tag{18}$$

where A_i, B_i, and C_i are tabulated empirical constants given in Table 1. The viscosity of the mixture is then found from Wilke's formulation [54]:

$$\mu = \sum_{i=1}^{NS} \frac{X_i \mu_i}{\sum_{j=1}^{NS} X_j \phi_{ij}} \tag{19}$$

$$\phi_{ij} = \frac{\left[1 + \left(\frac{\mu_i}{\mu_j}\right)^{\frac{1}{2}} \left(\frac{\mathcal{M}_j}{\mathcal{M}_i}\right)^{\frac{1}{4}}\right]^2}{\left[8\left(1 + \frac{\mathcal{M}_i}{\mathcal{M}_j}\right)\right]^{\frac{1}{2}}} \tag{20}$$

where $\mathcal{M}_i$ is the molecular weight of species i, and X_i is the mole fraction of species i. The individual species translational heat conduction coefficients (κ_{ti}) are given by Eucken's relation [48]:

$$\kappa_{ti} = \frac{5}{2} \mu_i c_{vti} \tag{21}$$

where

$$c_{vti} = \frac{3}{2} R_i \tag{22}$$

The overall coefficient is calculated by using Wilke's formula similar to the viscosity coefficient [6]. The thermal conductivities associated with the rotational and vibrational modes are given by [44]:

$$k_{(v,r)} = \sum_{i=1}^{nd} \frac{X_i k_{(v,r)i}}{\sum_{j=1}^{NS} X_j \phi_{ij}} \tag{23}$$

where ϕ_{ij} is the same as those used in Wilke's mixture rule for viscosity [54], and the sums are taken over the diatomic species only and:

$$\kappa_{ri} = \mu_i R_i \tag{24}$$

$$\kappa_{vi} = \mu_i \frac{R_i (\theta_{vi}/T_v)^2 e^{\theta_{vi}/T_v}}{(e^{\theta_{vi}/T_v} - 1)^2} \tag{25}$$

The mass diffusion coefficient is taken to be the same for all species, $D_i = D$ and is found by assuming a constant Schmidt number [47]:

$$Sc = \frac{\mu}{\rho D} = 0.5 \tag{26}$$

3.5 Source terms

The energy transfer modes considered are translation-vibration coupling and vibration-dissociation coupling. Other modes were assumed to be negligible in their effect [47]. Vibration-translation interactions are modeled using the Landau-Teller model [48]:

$$Q_{T-V} = \sum_{j=1}^{nd} \frac{\rho_j R_j \theta_{vj} \left(\frac{1}{e^{\theta_{vj}/T_t} - 1} - \frac{1}{e^{\theta_{vj}/T_v} - 1}\right)}{\tau_{vj}} \tag{27}$$

For the vibrational relaxation time of species j, τ_{vj}, the corrected Millikan and White formula [55] as proposed by Park [42] was used. This gives the vibrational time as:

$$\tau_{vj} = < \tau_{vj} > + \tau_{cj} \tag{28}$$

with

$$< \tau_{vj} > = \frac{\sum_{i=1}^{NS} X_i}{\sum_{i=1}^{NS} X_i / \tau_{vij}^{MW}} \tag{29}$$

where X_i is the mole fraction of species i.

τ_{vij}^{MW} is the Millikan and White relaxation time derived from empirical data [55], and is given by:

$$\tau_{vij}^{MW} = \frac{1}{p} \exp \left[1.16 \times 10^{-3} \mu_{ij}^{\frac{1}{2}} \theta_{vj}^{\frac{4}{3}} \left(T_t^{-\frac{1}{3}} - 0.015 \mu_{ij}^{\frac{1}{4}}\right) - 18.42\right] \tag{30}$$

where p is in units of atmospheres, θ_{vj} is the characteristic vibrational temperature of species j, and μ_{ij} is the reduced mass given by:

$$\mu_{ij} = \frac{\mathcal{M}_i \mathcal{M}_j}{\mathcal{M}_j + \mathcal{M}_i}, \tag{31}$$

The correction factor is given by:

$$\tau_{cj} = \frac{1}{\bar{c}_j \sigma_v N} \tag{32}$$

where $\bar{c}_j$ is the mean molecular speed given by:

$$\bar{c}_j = \sqrt{\frac{8 R_j T_t}{\pi}}, \tag{33}$$

σ_v is the limited collision cross section (in m^2) given by [56,57]:

$$\sigma_v = 10^{-21}\left(\frac{50,000}{T_t}\right)^2, \quad (34)$$

and N is the total number density of the gas. The model used for vibration-dissociation coupling is the one employed by Candler in Reference [46] and is given by

$$Q_{V-D} = \sum_{j=1}^{nd} w_j \frac{R_j \theta_{vj}}{e^{\theta_{vj}/T_v} - 1} \quad (35)$$

The total vibrational source term is then:

$$w_v = Q_{T-V} + Q_{V-D} \quad (36)$$

Chemistry is modeled by using a five species model (N_2, O_2, NO, N, O). Here, ionization is ignored. The five species reaction model is given as:

$$N_2 + M_i \rightleftharpoons N + N + M_i \quad (37)$$
$$O_2 + M_i \rightleftharpoons O + O + M_i \quad (38)$$
$$NO + M_i \rightleftharpoons N + O + M_i \quad (39)$$
$$N_2 + O \rightleftharpoons NO + N \quad (40)$$
$$NO + O \rightleftharpoons O_2 + N \quad (41)$$

where M_i denotes any of the i species. In general, the rate of formation of a reactant species in a general reaction of the form:

$$A + B \rightleftharpoons C + D \quad (42)$$

can be written as:

$$\mathcal{R} = k_b [A][B] - k_f [C][D] \quad (43)$$

Two chemical models for the rate coefficients (the k_f and k_b's) are used. The first model is the Dunn-Kang rate coefficients based on a two-temperature modle as presented by Häuser, *et al.* [45] The backward and forward coefficients are calculated using a modified Arrhenius expression of the form:

$$k = C T_x^{-\eta} exp(\theta_d / T_x) \quad (44)$$

where C, T_x, η, and θ_d for each reaction are given in Tables 2 and 3. The second model is the Park chemistry model for air [42,58]. In this model, only the forward rate coefficients are explicitly calculated by a modified Arrhenius equation similar to that used in the Dunn-Kang model. The backward rate coefficients are then deduced from the forward rates using the equilibrium constant:

$$k_b = k_f / K_{eq} \quad (45)$$

The equilibrium constants, K_{eq}, are given by empirical curve fits with respect to temperature. Coefficient and curve fit values for a wide range of reactions of interest in hypersonics are tabulated in the various works of Park [42,56,58].

4 Boundary Conditions

All flows studied here are wall bounded in some way, usually by a body immersed in a freestream. Because of this, wall boundary conditions to simulate the viscous interaction between the flowfield and the solid body are required. The no-slip condition for velocity and adiabatic wall condition for temperature are used as the flows examined are within the continuum regime. Isothermal walls are also used as they are a common way to simulate cooled walls without solving the conjugate heat transfer problem. Noncatalytic wall is used in the present study.

5 Numerical Methods

Once the physical model is defined, an associated numerical model suitable for computational simulations is needed. Often, methods are used for the spatial and temporal discretizations. Care must be taken to ensure that the scheme chosen is both stable and accurate. In particular, the terms associated with the nonequilibrium thermophysics have such small time scales associated with them, that they can add a high degree of numerical stiffness to the temporal discretization and special care must be taken when integrating in time. In order to capture all time and length scales associated with transient hypersonic nonequilibrium flow, high-order accurate CFD methods are required.

5.1 High-order shock fitting methods

The use of shock fitting method make it possible to use high-order difference scheme for spatial discretization. The general curvilinear three-dimensional coordinates (ξ, η, ζ, τ) are used along the body fitted grid lines (Fig. 2).

Shock fitting methods are used to treat the bow shock as a computational boundary. The Rankine-Hugoniot relations across the shock are used. When the thickness of shock is assumed to be infinitesimal, frozen flow can be used, which means there is no chemical reaction and vibrational excitation across the the shock. The Rankine-Hugoniot relations are similar to perfect gas results. The transient movement of the shock and its interaction with disturbance waves are solved as part of the solutions. Therefore, the grid surface of η = constant is unsteady due to the shock movement, but the grid surfaces of ξ = constant and ζ = constant are fixed plane surfaces during the calculations. In particular, the ξ = constant surface is generated such that they are normal to the wall surface. Therefore, only the η = constant grid lines change when the bow shock moves. In conservative form, the equations of motion can be written as:

$$\frac{\partial \mathbf{U}}{\partial t} + \frac{\partial}{\partial x}(\mathbf{F_1} + \mathbf{F_{v1}}) + \frac{\partial}{\partial y}(\mathbf{F_2} + \mathbf{F_{v2}}) + \frac{\partial}{\partial z}(\mathbf{F_3} + \mathbf{F_{v3}}) = \mathbf{W} \tag{46}$$

where the conserved quantity and source term vectors are:

$$\mathbf{U} = \begin{bmatrix} \rho_1 \\ \rho_2 \\ \rho_3 \\ \rho_4 \\ \rho_5 \\ \rho u \\ \rho v \\ \rho w \\ E_v \\ E \end{bmatrix}, \qquad \mathbf{W} = \begin{bmatrix} w_1 \\ w_2 \\ w_3 \\ w_4 \\ w_5 \\ 0 \\ 0 \\ 0 \\ w_v \\ 0 \end{bmatrix} \tag{47}$$

Inviscid fluxes are

$$\mathbf{F_1} = \begin{bmatrix} \rho_1 u \\ \rho_2 u \\ \rho_3 u \\ \rho_4 u \\ \rho_5 u \\ \rho u^2 + p \\ \rho uv \\ \rho uw \\ uE_v \\ u(E+p) \end{bmatrix}, \quad \mathbf{F_2} = \begin{bmatrix} \rho_1 v \\ \rho_2 v \\ \rho_3 v \\ \rho_4 v \\ \rho_5 v \\ \rho uv \\ \rho v^2 + p \\ \rho vw \\ vE_v \\ v(E+p) \end{bmatrix},$$

$$\mathbf{F_3} = \begin{bmatrix} \rho_1 w \\ \rho_2 w \\ \rho_3 w \\ \rho_4 w \\ \rho_5 w \\ \rho uw \\ \rho vw \\ \rho w^2 + P \\ wE_v \\ w(E+p) \end{bmatrix} \tag{48}$$

Viscous and diffusive fluxes are

$$\mathbf{F_{v1}} = \begin{bmatrix} j_{1x} \\ j_{2x} \\ j_{3x} \\ j_{4x} \\ j_{5x} \\ -\tau_{xx} \\ -\tau_{xy} \\ -\tau_{xz} \\ q_{vx} \\ Q_x \end{bmatrix}, \qquad \mathbf{F_{v2}} = \begin{bmatrix} j_{1y} \\ j_{2y} \\ j_{3y} \\ j_{4y} \\ j_{5y} \\ -\tau_{xy} \\ -\tau_{yy} \\ -\tau_{yz} \\ q_{vy} \\ Q_y \end{bmatrix},$$

$$\mathbf{F_{v3}} = \begin{bmatrix} j_{1z} \\ j_{2z} \\ j_{3z} \\ j_{4z} \\ j_{5z} \\ -\tau_{xz} \\ -\tau_{yz} \\ -\tau_{zz} \\ q_{vz} \\ Q_z \end{bmatrix} \tag{49}$$

where

$$\begin{aligned} Q_x &= -u\tau_{xx} - v\tau_{xy} - w\tau_{xz} + q_x \\ Q_y &= -u\tau_{xy} - v\tau_{yy} - w\tau_{yz} + q_y \\ Q_z &= -u\tau_{xz} - v\tau_{yz} - w\tau_{zz} + q_z \end{aligned} \tag{50}$$

The transformation relations for the current grid systems are

$$\begin{cases} \xi = \xi(x,y,z) \\ \eta = \eta(x,y,z,t) \\ \zeta = \zeta(x,y,z) \\ \tau = t \end{cases} \Longleftrightarrow \begin{cases} x = x(\xi,\eta,\zeta,\tau) \\ y = y(\xi,\eta,\zeta,\tau) \\ y = y(\xi,\eta,\zeta,\tau) \\ t = \tau \end{cases} \quad (51)$$

where $\xi_t = 0$ and $\zeta_t = 0$ because the ξ and ζ grid lines are fixed when the shock boundary moves. In the numerical simulations, the governing equation (46) are transformed into the computational domain (ξ, η, ζ, τ) as follows

$$\frac{1}{J}\frac{\partial U}{\partial \tau} + \frac{\partial F_1'}{\partial \xi} + \frac{\partial F_2'}{\partial \eta} + \frac{\partial F_3'}{\partial \zeta} + \frac{\partial F_{1v}'}{\partial \xi} + \frac{\partial F_{2v}'}{\partial \eta} + \frac{\partial F_{3v}'}{\partial \zeta} + U\frac{\partial (\frac{1}{J})}{\partial \tau} = \frac{W}{J} \quad (52)$$

where

$$F_1' = \frac{F_1\xi_x + F_2\xi_y + F_3\xi_z}{J} \quad (53)$$

$$F_2' = \frac{F_1\eta_x + F_2\eta_y + F_3\eta_z + U\eta_t}{J} \quad (54)$$

$$F_3' = \frac{F_1\zeta_x + F_2\zeta_y + F_3\zeta_z}{J} \quad (55)$$

$$F_{1v}' = \frac{F_{v1}\xi_x + F_{v2}\xi_y + F_{v3}\xi_z}{J} \quad (56)$$

$$F_{2v}' = \frac{F_{v1}\eta_x + F_{v2}\eta_y + F_{v3}\eta_z}{J} \quad (57)$$

$$F_{3v}' = \frac{F_{v1}\zeta_x + F_{v2}\zeta_y + F_{v3}\zeta_z}{J} \quad (58)$$

where J is the Jacobian of the coordinate transformation, and ξ_x, ξ_y, ξ_z, η_x, η_y, η_z, η_t, ζ_x, ζ_y, and ζ_z are the grid transformation metrics, which are computed as functions of the body shape, the grid-point distribution along the grid lines, the wall-normal distance $H(\xi,\zeta,\tau)$ between the shock and the wall along the η grid lines (see Fig. 2), and the time derivative H_τ. These metrics functions are functions of time through H and H_τ which can be solved simultaneously with the interior flow variables. This is described in more detail in Reference [59]. Fifth-order upwind finite difference scheme carried out in stretched physical grid without using the coordinate transformation is applied to convective terms for the purpose of numerical stability consideration, while sixth-order central schemes based on coordinate transformation are applied for the discretization of viscous terms [35].

5.2 Semi-implicit Runge-Kutta method

The spatial discretization of the governing equations leads to a system of first-order ordinary differential equations. Third-order Semi-implicit Runge-Kutta scheme [34] is used for temporal discretization, which split the governing equations into non-stiff terms resulting from spatial discretization of the flux terms that can be treated by explicit Runge-Kutta method and stiff terms containing the thermal-chemical source terms that need to be simultaneously treated by implicit Runge-Kutta method. Details of these method is described in Reference [34]. For numerical simulation with source term, it is necessary to exactly evaluate the Jacobian of source vector $\mathbf{C} = \partial\mathbf{W}/\partial\mathbf{U}$. $\mathbf{W}$ can be expressed as a function of the temperature

$$\mathbf{W}(\mathbf{U}) = \tilde{\mathbf{W}}(\mathbf{U}, T(\mathbf{U}), T_v(\mathbf{U})), \quad (59)$$

and Jacobian can be written as

$$\mathbf{C} = \frac{\partial \tilde{\mathbf{W}}}{\partial \mathbf{U}} + \frac{\partial \tilde{\mathbf{W}}}{\partial T}\frac{\partial T}{\partial \mathbf{U}} + \frac{\partial \tilde{\mathbf{W}}}{\partial T_v}\frac{\partial T_v}{\partial \mathbf{U}} \quad (60)$$

The derivation of each term in more detail can be found in Reference [47]

6 Numerical Results

This numerical method and computational code is tested by computing steady hypersonic flow over a cylinder. Numerical accuracy is estimated by grids refinement. Heat transfer on the surface, vorticity jump across the shock and real gas effects on stability of transient hypersonic flow over parabolas are investigated.

6.1 Code validation and numerical accuracy

Steady hypersonic reacting flow past cylinders based on Hornung's [36] experimental data is computed as a test case. The partially dissociated nitrogen flow past a 2 inches diameter cylinder with $u_\infty = 5590\ m/s$, $T_\infty = 1833°K$, $p_\infty = 2910\ Pa$, 92.7% N_2 and 7.3% N by mass, $T_w = 1833°K$ and a Reynolds number of 6000 is studied. The flow conditions replicate those studied experimentally by Hornung and computationally by Furomoto [37]. Except specification of other flow

conditions, all results shown in this section are based on above flow conditions. Interferograms were made in of flow field in this case. The density change, $\triangle\rho$ is related to the fringe shift F by:

$$\triangle\rho = \frac{4160F\lambda}{L(1.0+0.28C_N)} kg/m^3 \quad (61)$$

where F is the fringe number, L is the geometrical path in experiment, λ is the wavelength, C_N is mass fraction of atomic nitrogen, and $\triangle\rho = \rho - \rho_\infty$. In Hornung's [36] experiment, the fringe number of photograph is taken at $\lambda = 5.330^{-7}m$, L = 0.1524 m. The fringe pattern gives a qualitative picture of the density pattern provided that C_N does not change too much. In numerical simulation, to convert computational result to interferogram, one way to do it is to plot the contours of constant fringe nubmer, $(\cos(\pi F))^2$.

6.1.1 Comparison with experimental results

Two chemistry models were used for this case to test their effectiveness in the simulation of reacting hypersonic flows. The first model was Dunn-Kang rate coefficient model [45], and the second model Park model [42]. Figure 3 compares computational results using the Park model and Dunn-Kang model (shown in the bottom half of the figure), to an experimental interferogram published by Hornung [36] (shown in the top half of the figures). The computational shock shape and standoff distance agree very well with the experimental data. The inference fringes shapes of Park Model are very similar to experimental photo. For the result of Dunn-Kang Model, there is visible differences between the inference fringes shapes of the computation and experiment. A comparison of fringe number profile along the stagnation line between the two chemical model is shown in Figure 4. Compared with experimental data, the Park model yielded better results than did the Dann-Kang model. As shown by Candler [60] , the choice of thermochemical model can have large effects on the shock shape and standoff distance. For flow over cylinders, it was demonstrated that including chemical nonequilibrium, but with only a one temperature (thermal equilibrium) model, did a very poor job in capturing the shock standoff distance and shape. The ability of the computations presented here to accurately capture the shock shapes and standoff distances, with only a modest difference in the shape of the interference fringes, demonstrates the capability of the code to accurately model flows in thermochemical nonequilibrium.

6.1.2 Comparison with other numerical results

The computational results are also compared with Furomoto's [37] computational results. Flow conditions and physical models in this case are same as Furumoto's computation. The only difference between this two computations is in numerical methods, where fifth-order shock-fitting method is used in this paper while second-order TVD shock-capturing method is used in Furumoto's computation. Comparison of computed contours of pressure, is shown in Fig. 5, in which Furumoto's computational results are shown in the bottom half of these figures while computational results of this paper are show in the top half of these figures. The comparison shows that the computational results by different numerical methods are in good agreement with each other. Small differences exist in the standoff distance of bow shock. The flow change immediately behind the shock by shock capturing method is not as smooth as that by shock-fitting method which is shown in the contours of pressure. This is due to the different grid distribution and numerical methods. In current computation, stretching grids in both shock layer and boundary layer are used, while grids used by Furumoto are only stretching in boundary layer.

The chemically frozen and thermally nonequilibrium nitrogen flow past 2 meters diameter infinite cylinders with adiabatic wall are studied and compared with inviscid flow results by Giordano [39]. The flow conditions are given as following: $M_\infty = 6.5$, $T_\infty = 300°K$, $p_\infty = 50 or 500 Pa$. Viscous terms and thermal conduction effects are ignored in reference [39]. Figure 6 shows that our results match the results published by Giordano very well, and viscosity is negligible in these two cases.

6.1.3 Numerical accuracy

For simulation of viscous hypersonic nonequilibrium flows over blunt body, flow properties such as temperature, species mass fraction, and density may dramatically change in the shock layer immediately behind the shock and boundary layer near the body due to chemical reaction and wall conditions. If flow is thermally and chemically frozen, it is just necessary to cluster more grids in boundary layer because the change of flow properties in shock layer is smooth. Numerical experiment shows that stretching grids in both shock layer and boundary layer does not change the standoff distance of bow shock for frozen flow. But for nonequilibrium flow, there are steep changes in shock layer. If grid is stretching only in boundary layer, the standoff distance of bow shock can not be accurately com-

puted, and there is obvious spurious oscillation behind the shock. Grid refinement in both shock layer and boundary layer is necessary in order to cluster more grids point in the region where flow changes significantly, which is easier to carry out for shock-fitting method than shock-capturing method.

All computations presented here used 60 × 60 grid stretching in the body normal direction on both sides close body and shock respectively. Comparison of heat transfer and pressure on the body surface and contours of translational temperature computed with differents grids are shown in Fig. 7,8 and 9. Since the heat transfer at the surface, contours of vorticity, pressure, temperature, species mass fraction, and density in the flow field using 120 × 120 almost coincide with that using a 60×60 grid, and the computed pressure and heat transfer at the stagnation point, and maximum vorticity on the surface using the 120 × 120 grid were within %0.9, %1.5 and %1.2 respectively, it was concluded that the number of points was sufficient to resolve the shock layer and the boundary layer for the purpose of simulation of surface heating and flow properties, including density, velocity, pressure, temperature, species mass fraction, and their first-order derivatives.

6.2 Heat transfer in nonequilibrium flow

In the regime of Boundary layer flow and under the assumption of locally self-similar solutions, the partial differential NS quations reduce to ordinary differential ones which can be solved by Chebyshev spectral collocation method. The boundary conditions at the edge of the boundary layer can be obtained from directly numerical solutions discussed above. The purpose of this study is to compare the heat flux computed through NS equations and BL equations.

In a nonequilibrium hypersonic flow, the local heat flux on the isothermal wall is determined by sum of the conduction and diffusion components:

$$q_w = -(\kappa_t + \kappa_r)\frac{\partial T_t}{\partial n} - \kappa_v \frac{\partial T_v}{\partial n} + \sum_{i=1}^{NS} j_{in} h_i \qquad (62)$$

where n is direction normal to surface, and mass diffusion fluxes for species i are given by:

$$j_{in} = -\rho D_i \frac{\partial (\rho_i/\rho)}{\partial y} \qquad (63)$$

The surface heating is most serious near the stagnation point which is extensively studied in the past decades. Most of these studies are based on the classical theory of Fay and Riddell [61] and their numerical solution of boundary layer equations. For fully catalytic wall (chemically equilibrium is reached due to infinitely fast reaction), the heat transfer rate near the stagnation point is given in the following form [61]:

$$q = 0.570 P_r^{-0.6} (\rho_e \mu_e)^{0.4} (\rho_w \mu_w)^{0.1} \sqrt{\left(\frac{du_e}{dx}\right)_s} (h_e - h_w)\left[1 + (Le^{\alpha} - 1)\frac{h_d}{h_e}\right] \qquad (64)$$

where h_d is the energy in dissociation, subscript w refers to the wall, subscript e to the edge of the boundary layer, subscript s to the stagnation point, and the exponent α is 0.52 and 0.63 for equilibrium and frozen boundary layer respectively. For noncatalytic wall, the resultant heat-transfer could be given by Equation (64) with $L_e = 0$. These classical heat transfer correlations can be applicable under conditions summerized by Gökçen [62]. Our code based on Chebyshev Spectral collocation method for stagnation boundary layer flow is validated by calculating perfect gas flow. In this case, boundary conditions at the edge of boundary layer can approximately be given by using Rankine-Hugoniot relations, which is not related to the body geometry. The heat flux at stagnation point can be expressed as:

$$q = -\kappa_w \rho_w \left(\frac{2\rho_\infty}{\rho_e}\right)^{1/4} \sqrt{\frac{u_\infty}{r_0}} \left(\frac{\partial T}{\partial \eta}\right)_w \qquad (65)$$

where subscript w stands for the values at wall and expression of η for transformation can be found in reference [38]. The temperature gradient in normal wall direction is solved numerically. For fixed free steam parameters and wall temperature, all variables in equation (65)except for curvature radius, r_0, are constant, which indicates that q is in inverse proportion to r_0(shown in Fig. 10). In Fig. 10, heat flux is compared with Fay and Riddell's [38] curve fitted results and our numerical results based on NS equations and BL equations respectively. Here BL results are calculated with outside boundary condition obtained from NS results. Figure 10 shows that both of our NS results and BL results are in good agreement with Fay and Riddell's curve fitted results.

To establish an equilibrium boundary layer flow, the partially dissociated nitrogen flow past a 4cm diameter cylinder with $u_\infty = 4450\ m/s$, $T_\infty = 2326.4°K$, $p_\infty = 11400.0\ Pa$, 94.5% N_2 and 0.5% N by mass, $T_w = 2326.4°K$ is studied by solving NS equations and BL equations respectively. Same chemical model of reaction is used in both calculations. The boundary conditions of boundary layer are given by using Rankine-

Hugoniot relations. The profiles of mass fraction and temperature along the stagnation line are shown in Fig. 11 and 12. Here, equilibrium states are obtained by solving 1-D normal shock relations in equilibrium flows. In these two figures, both NS results and BL results predict the equilibrium states very well, while NS results and BL results agree with each other. It also shows that vibrational temperature equilibrates faster than mass fraction does.

Heat flux at stagnation point computed through NS equation and boundary layer equations respectively in different cases are showned in table 6. The flow conditions replicate Hornung [36] and Sanderson [63]'s experiment. The maximum difference in heat flux computed by these two methods are less than 15%.

6.3 Vibrationally relaxing flow of N_2 past a parabola

The chemically frozen and thermally nonequilibrium N_2 flow past a parabolic leadingedge with isothermal wall is studied. The receptivity of the 2-D boundary layer to weak freestream acoustic flow at zero angle of attack are considered. As comparison, corresponding perfect gas flow is also studied. All results shown in this section are obtained by using a set of 160 grids. The body surface is a parabola given by

$$x = by^2 - d \tag{66}$$

where b a given constant and d is taken as the reference length. The body surface is assumed to be a non-slip wall with an isothermal wall temperature T_w.

The specific flow conditions are:

$M_\infty = 15$	$\epsilon = 1.0 \times 10^{-3}$
$T_\infty = 250.0\,K$	$p_\infty = 20.3\,Pa$
$T_w = 1000\,K$	$\gamma = 1.4$
$R = 296.93\,Nm/kgK$	$Pr = 0.72$
$b = 40\,m^{-1}$	$d = 0.1\,m$

Nose Radius of Curvature $r = 0.0125\,m$
Imposed Acoustic Wave Number $k = 314.159$
$Re_\infty = \rho_\infty U_\infty d/\mu_\infty = 8524.6$

6.3.1 Steady flow solutions

It has been found that the accuracy of the stability analysis for hypersonic boundary layers is very sensitive to the accuracy of the mean flow solutions [64]. High accuracy mean flow solutions are critical for study of receptivity as well as for the LST analyses.

Figure 13 shows the comparison of entropy contours and boundary layer developing between vibrationally relaxing flow and perfect gas flow. In the vicinity of stagnation line, shock angle is nearly upright, so temperature behind the shock is so high that vibrational energy of diatomic molecues is excited. As a result, more entropy is generated compared with perfect gas flow. Therefore, the entropy layer in this region is much thicker than that in the same region of perfect gas flow field. Based on Reshotko and Khan [65]'s results, the entropy layer will be swallowed by boundary layer with developing, which plays an important role in the stability and transition of boundary layer downstream.

Figure 14 shows the profile of translational temperature and vibrational temperature along the stagnation line. Because of the low density, length scale of vibrational relaxation is in the same order as standoff distance of shock although the translational temperature is very high behind the shock.

6.3.2 Receptivity of hypersonic nonequilibrium flow

In the simulation, the freestream disturbances are superimposed on the steady mean flow to investigate the development of T-S waves in the boundary layer with the effects of the bow shock interaction. The wave field of the unsteady viscous flows are represented by the perturbations of instantaneous flow variables with respect to their local mean variables. For example, the instantaneous velocity perturbation u' is defined as the perturbations with respect to local mean velocity, i.e.,

$$u' = u'(x, y, t) = u(x, y, t) - U(x, y) \tag{67}$$

where $U(x, y)$ is the mean flow velocity. The freestream disturbances are assumed to be weak monochromatic planar acoustic waves with wave front normal to the center line of the body. The perturbations of flow variable introduced by the freestream acoustic wave before reaching the bow shock can be written in the following form:

$$\begin{Bmatrix} u' \\ v' \\ p' \\ \rho' \end{Bmatrix}_\infty = \begin{Bmatrix} |u'| \\ |v'| \\ |p'| \\ |\rho'| \end{Bmatrix}_\infty e^{ik[x-(1+M_\infty^{-1})t]} \tag{68}$$

where $|u'|$, $|u'|$, $|p'|$, and $|\rho'|$ are perturbation amplitudes satisfying the following relations:

$$|u'|_\infty = u_\infty \epsilon\,, \qquad |v'|_\infty = 0$$
$$|p'|_\infty = \rho_\infty C_\infty |u'|\,, \qquad |\rho'|_\infty = |p'|_\infty / C_\infty^2$$

where ϵ represents the freestream wave magnitude, which is a small number. The parameter k is the freestream wave number which is related to the circular frequency ω by:

$$\omega = k\,(c_\infty + u_\infty) \tag{69}$$

The unsteady calculations are carried out for 20 periods in time so that the solutions reach a periodic state. The accuracy of unsteady flow is verified by comparing the vorticity jump across the bow shock with theoretical results which is shown in Fig. 15. Here, vorticity is normalized with respect to U_∞/d. The prediction of vorticity jump across the shock is described in the literature [66]. For unsteady hypersonic flow, the vorticity jump across the bow shock can expressed as following:

$$\Omega_s = (U_\infty, \frac{\partial \theta}{\partial s} + \frac{\partial v_s}{\partial s}) \frac{(1-\vartheta)^2}{\vartheta} \tag{70}$$

where, s is the direction along the shock, θ is the angle between shock and x-axis, and ϑ is the ratio of density across the shock, i.e. $\vartheta = \rho_\infty/\rho_s$. Because only momentum equation is used in the derivation of vorticity jump, this prediction is also valid for thermally and chemically nonequilibrium flows. The numerical results are in good agreement with theoretical prediction except that there exists visible difference which is due to viscous effects. Near the nose of the leading edge, the standoff distance of bow shock is less than that of downstream, where viscous effects are more obvious.

Any freestream waves interacting with the bow shock in hypersonic flow always generate a combination of all three kinds of waves, namely acoustic (pressure), entropy, and vorticity waves. The acoustic wave is propagated with the sound speed relative to the moving fluid, while the entropy and vorticity waves convect with the moving fluid velocity. The interaction between external waves and $T-S$ waves in boundary layer is discussed in literature [67]. In this paper, we mainly focus on the real gas effect on these three kinds of waves. The contours of phase angle of pressure, vorticity and entropy perturbation are plotted in Fig. 16. From this figure, it is reasonable to draw a conclusion that the vibrational relaxation does not obviously effect the acoustic waves, while it significantly effects the properties of entropy and vorticity waves. Although vibrational relaxation mainly concentrates in the region near the nose of leading edge, the entropy and vorticity waves are strongly effected both in the leading edge region and downstream region. The instantaneous perturbation contours of pressure, temperature, vertical velocity, and entropy are shown in Fig. 17, 18, 19 and 20 respectively, while corresponding contours of perfect gas are drawn together. The distribution of the Fourier amplitude and phase angle of entropy and vorticity perturbations along the parabola surface are shown in Fig.21 and 22 For perfect gas, according to the results published by Zhong [67], instability mode is first mode dominated before $X < -0.6$ while it switchs to second mode dominated after $x > -0.6$ in this specific case. For real gas, Malik [25] has proved that real gas effects stablize the first mode instability while destabilize the higher mode. The recognizaton of different stability modes and the response to real gas effects need further study including linear stability analyses.

6.4 Chemically reacting flow of O_2 past a parabola

The chemically and thermally nonequilibrium O_2 flow past a parabolic leadingedge with isothermal wall is considered. The receptivity of the 2-D boundary layer to weak freestream acoustic flow at zero angle of attack are studied.

The specific flow conditions are:

$M_\infty = 15$ $\qquad \epsilon = 1.0 \times 10^{-3}$
$T_\infty = 200.0\,K$ $\qquad p_\infty = 41.2\,Pa$
$T_w = 1000\,K$ $\qquad Pr = 0.72$
$b = 40\,m^{-1}$ $\qquad d = 0.1\,m$
Nose Radius of Curvature $r = 0.0125\,m$
Imposed Acoustic Wave Number $k = 314.159$
$Re_\infty = \rho_\infty U_\infty d/\mu_\infty = 6213$

6.4.1 Steady flow solutions

Dunn-Kang Model are used for the study of reacting O_2 flow. The profiles of temperature and mass fraction along the stagnation line are shown in Fig. 23. Vibrational temperature overshoot the translational temperature because dissociation of diatomic O_2 apportions energy between them. It also showed that the time scale of vibrational relaxtion is less than that of chem-

ical relaxtion. The contours of atomic oxygen and entropy are shown in Fig. 24.

6.4.2 Unsteady flow solutions

Figure 25 shows the vorticity jump across unsteady bow shock. Compared with the vorticity jump without chemical reaction above, higher maximum vorticity are generated due to the dissociation of diatomic oxygen, which can lead more unstable layers by a qualitative analysis. The computational results agree with theoretical prediction very well. The instantaneous perturbation contours of temperature, pressure, vertical velocity, and entropy are shown in Fig. 26 The real gas effects on stability analyses are ongoing.

7 Conclusions

This paper has applied and tested a high-order upwind finite difference shock fitting method for the simulation of nonequilibrium hypersonic flows with strong bow shock. The validation of our code is conducted by comparison of our computational results with experimental results as well as other numerical results. The ability of the computations presented in this paper to accurately capture the shock shapes and the standoff distances demonstrates the capability of the code to sufficiently model flows in thermochemical nonequilibrium. Grids refinement in both shock layer and boundary layer makes it possible to capture the sharp changes of flow variables in these regions. Comparison of numerical results based on both course and refined grids shows that the results are grids independent. Investigation of heat flux at the stagnation point in hypersonic flow over blunt body shows that our code can effectively predicate the wall heating. Vibrationally relaxing N_2 flow and dissociating O_2 flow over parabolas and corresponding receptivity to superimposed acoustic wave in freestream are studied by applying this method. Work is currently underway to analyze the real gas effects on the stability of hypersonic flow.

8 Acknowledgements

This research was supported by the Air Force Office of Scientific Research under grant numbers F49620-94-1-0019 and F49620-95-1-0405 monitored by Dr. Len Sakell.

References

[1] J. D. Anderson. *Hypersonic and High Temperature Gas Dynamics.* McGraw-Hill, 1989.

[2] T.A. Herzfeld, K. F. Litovitz. *Absorption and Dispersion of Ultrsonic Waves.* New York, Academic Press, 1959.

[3] C. Park. On convergence of chemically reacting flows. *AIAA Paper 85-0247*, 1985.

[4] Goulard R. On catalytic recombination rates in hypersonic stagnation heat transfer. *Jet Propulsion*, 28(11):733–745, 1958.

[5] C. Park. *Nonequilibrium Hypersonic Aerothermodynamics.* Wiley Interscience, 1990.

[6] J. D. Anderson Jr. *Hypersonic and High Temperature Gas Dynamics.* McGraw-Hill, Inc., 1989.

[7] H. K. Cheng. Recent advances in hypersonic flow research. *AIAA Journal*, 1:295–310, 1963.

[8] H. K. Cheng. Perspectives on hypersonic viscous flow research. *Annu. Rev. Fluid Mechanics*, 25, 1993.

[9] M. Rasmussen. *Hypersonic Flow.* John Wiley and Sons, Inc., 1994.

[10] H. K. Cheng. Perspective on hypersonic nonequilibrium flow. *AIAA Journal*, 33:385–400, 1995.

[11] J.J. Bertin. *Hypersonic Aerothermodynamics.* Washington, DC, 1994.

[12] Th. Herbert and M. V. Morkovin. Dialogue on Bridging Some Gaps in Stability and Transition Research. *In Laminar-Turbulent Transition, IUTAM Symposium, Stuttgart, Germany, 1979, R. Eppler, H. Fasel, Editors, pp. 47-72*, Springer-Verlag Berlin, 1980.

[13] M. V. Morkovin and E. Reshotko. Dialogue on Progress and Issues in Stability and Transition Research. *In Laminar-Turbulent Transition, IUTAM Symposium, Toulouse, France, 1989, D. Arnal, R. Michel, Editors*, Springer-Verlag Berlin, 1990.

[14] E. Reshotko. Boundary Layer Instability, Transition and Control. *AIAA paper 94-0001*, 1996.

[15] Th. Herbert. Progress in Applied Transition Analysis. *AIAA paper 96-1993*, 27th AIAA Fluid Dynamics Conference, New Orleans, LA, June, 1996.

[16] D. Bushnell. Notes on Initial Disturbance Field for the Transition Problem. *Instability and Transition, Vol. I*, M. Y. Hussaini and R. G. Viogt, editors, pp. 217-232, Springer-Verlag, 1990.

[17] M. Morkovin. On the Many Faces of Transition. *Viscous Drag Reduction*, C.S. Wells, editor, Plenum, 1969.

[18] L. M. Mack. Linear Stability Theory and the Problem of Supersonic Boundary-Layer Transition. *AIAA Journal*, Vol. 13, No. 3, pp. 278-289, 1975.

[19] L. M. Mack. Boundary layer linear stability theory. In *AGARD report, No. 709*, 1984.

[20] W. S. Saric. Götler Vortices. *Annual Review of Fluid Mechanics*, Vol. 26, pp. 379-409, 1994.

[21] H. L. Reed and W. S. Saric. Stability of Three-Dimensional Boundary Layers. *Annual Review of Fluid Mechanics*, Vol. 21, pp. 235-284, 1989.

[22] M. Nishioka and M. V. Morkovin. Boundary-Layer Receptivity to Unsteady Pressure Gradients: Experiments and Overview. *Journal of Fluid Mechanics*, Vol. 171, pp. 219-261 1986.

[23] M. E. Goldstein and L. S. Hultgren. Boundary-Layer Receptivity to Long-Wave Free-Stream Disturbances. *Annual Review of Fluid Mechanics*, Vol. 21, pp. 137-166 1989.

[24] W. S. Saric, H. L. Reed, and E. J. Kerschen. Leading edge receptivity to sound: Experiments, dns, and theory. *AIAA Paper 94-2222*, 1994.

[25] M. R. Malik and E. C. Anderson. Real Gas Effects on Hypersonic Boundary-Layer Stability. *Physics of Fluids A*, Vol. 3, No. 5, pp. 803-19, 1991.

[26] M. R. Malik. Transition in Hypersonic Boundary Layers. Fourthe Symposium on Numerical and Physical Aspects of Aerodynamic FLows, January 16-19, 1989,State University, Long Beach, CA. .

[27] G. S. Stuckert and H. L. Reed. Linear Disturbances in Hypersonic, Chemically Reacting Shock Layers. *AIAA Journal*, Vol. 32, No. 7, pp. 1384-1393, 1994.

[28] M. L. Hudson, N. Chokani, and G. V. Candler. Nonequilibrium effects on hypersonic boundary layers and inviscid stability. *AIAA Paper 94-0852*, 1994.

[29] M. L. Hudson, N. Chokani, and G. V. Candler. Linear stability of hypersonic flow in thermochemical nonequilibrium. *AIAA Paper 96-0671*, 1996.

[30] H. Vinh C.-L. Chang and M.R. Malik. Hypersonic boundery-layer stability with chemical reactions using pse. *AIAA paper 97-2012*, 1997.

[31] J. M. Kendall. Wind Tunnel Experiments Relating to Supersonic and Hypersonic Boundary-Layer Transition. *AIAA Journal*, Vol. 13, No. 3, pp. 290-299, 1975.

[32] J. M. Kendall. Experiments on Boundary-Layer Receptivity to Freestream Turbulence. *AIAA Paper 98-0530*, 1998.

[33] Philippe H. Adam and Hans G. Hornung. Enthalpy effects on hypervelocity boundary layer transition: Experiments and free flight data. *AIAA paper 97-0764*, January 1997.

[34] X. Zhong. Direct Numerical Simulation of Hypersonic Boundary-Layer Transition Over Blunt Leading Edges, Part I: New Numerical Methods and Validation . *AIAA paper 97-0755, 35th AIAA Aerospace Sciences Meeting and Exhibit, January 6-9, Reno, Nevada*, 1997.

[35] X. Zhong. High-Order Finite-Difference Schemes for Numerical Simulation of Hypersonic Boundary-Layer Transition. *Journal of Computational Physics*, 1998. Submitted.

[36] H. G. Hornung. Non-equilibrium dissociating nitrogen flow over spheres and circular cylinders. *Journal of Fluid Mechanics*, 53:149–176, 1972.

[37] G. Furumoto. *Unsteady Shock-Wave Reflection and Interaction in Viscous Flow with Thermal and Chemical Nonequilibrium*. PhD thesis, University of California, Los Angeles, June 1997.

[38] F.R. Riddell J.A. Fay. Theory of Stagnation Point Heat Transfer in Dissociated Air . *Journal of The Aeronautical Sciences*, 25(2):73–85, February 1958.

[39] D. Giordano. Vibrationally relaxing flow of n_2 past an infinite cylinder. *Journal of Thermophysics and Heat Transfer*, 11:27–35, 1997.

[40] W. G. Vincenti and W. G. Kruger Jr. *Introduction to Physical Gas Dynamics*. Krieg, 1965.

[41] J. F. Clarke and M. McChesney. *The Dynamics of Real Gases*. Butterworths, 1964.

[42] C. Park. *Nonequilibrium Hypersonic Aerothermodynamics*. Wiley Interscience, 1990.

[43] J. H. Lee. Basic governing equations for the flight regimes of aeroassisted orbital transfer vehicles. Technical Report AIAA Paper 84-1729, 1984.

[44] R.N. Gupta, J. M. Yos, R. A. Thompson, and K. P. Lee. *A Review of Reaction Rates and Thermodynamic Transport Properties for an 11-Species*

Air Model for Chemical and Thermal Nonequilibrium Calculations to 30000K. NASA RP-1232, 1990.

[45] J. Häuser, J. Muylaret, H. Wong, and W. Berry. Computational aerothermodynamics for 2d and 3d space vehicles. In T. K. S. Murthy, editor, *Computational Methods in Hypersonic Aerodynamics.* Kluwer Academic Publishers, 1991.

[46] G. V. Candler. *The Computation of Weakly Ionized Hypersonic Flows in Thermo-Chemical Nonequilibrium.* PhD thesis, Stanford University, 1988.

[47] T. Gökçen. *The Computation of Hypersonic Low Density Flows with Thermochemical Nonequilibrium.* PhD thesis, Stanford University, 1989.

[48] W. G. Vincenti and C. H. Kruger. *Introduction to Physical Gas Dynamics.* John Wiley and Sons, Inc., 1965.

[49] R. B. Bird, W. E. Stewart, and E. N. Lightfoot. *Transport Phenomena.* John Wiley and Sons, 1960.

[50] J. O. Hirschfelder, C. F. Curtiss, and R. B. Bird. *Molecular Theory of Gases and Liquids.* John Wiley and Sons, 1954.

[51] F. G. Blottner. Finite difference methods of solution of the boundary-layer equations. *AIAA Journal*, 8:193–205, 1970.

[52] J. Cousteix, D. Arnal B. Aupoix, J. P. Brazier, and A. Lafon. Shock layers and boudnary layers in hypersonic flows. *Progress in Aerospace Sciences*, pages 95–212, 1994.

[53] J. N. Moss, G. A. Bird, and V. K. Dorga. *Nonequilibrium Thermal Radiation for an Aerospace Flight Experiment Vehicle.* AIAA Paper 88-0081, 1988.

[54] C. R. Wilke. A viscosity equation for gas mixtures. *Journal of Chemical Physics*, 18(4):517–519, 1950.

[55] R. C. Millikan and D. R. White. Systematics of vibrational relaxation. *Journal of Chemical Physics*, 12:3209–3213, 1963.

[56] C. Park. Assessment of two-temperature kinetic model for ionizing air. *Journal of Thermophysics and Heat Transfer*, 3:233–244, 1989.

[57] L. C. Hartung, R. A. Mitcheltree, and P. A. Gnoffo. Coupled radiation effects in thermochemical nonequilibrium shock-capturing flowfield calculations. *Journal of Thermophysics and Heat Transfer*, 8:244–250, 1994.

[58] C. Park. Review of chemical-kinetic problems of future nasa missions, i: Earth entries. *Journal of Thermophysics and Heat Transfer*, 7:385–398, 1993.

[59] X. Zhong. High-Order Finite-Difference Shock-Fitting Schemes for Direct Numerical Simulation of Hypersonic Boundary-Layer Receptivity to Free-Stream Disturbances. *Presented at the First AFOSR Conference on Dynamic Motion CFD, New Brunswick, New Jersey, June 3-5*, 1996.

[60] G. V. Candler. *On the Computation of Shock Shapes in Nonequilibrium Hypersonic Flows.* AIAA Paper 89-0312, 1989.

[61] J. A. Fay and F. R. Riddell. Theory of stagnation point heat transfer in dissociated air. *Journal of the Aeronautical Sciences*, 25:73–85, 1958.

[62] T. Gökçen. Effects of freestream nonequilibrium on convective heat transfer to a blunt body. *Journal of Thermophysics and Heat Transfer*, 10(2):234–241, 1996.

[63] S. R. Sanderson. *Shock Wave Interaction in Hypervelocity Flow.* PhD thesis, California Institute of Technology, 1995.

[64] Th. Herbert and V. Esfahanian. Stability of Hypersonic Flow over a Blunt Body. *AGARD CP-514*, pp. 28-1 – 12, April, 1993.

[65] E. Reshotko and N.M.S. Khan. Stability of the Laminar Boundary Layer on a Blunt Plate in Supersonic Flow. *IUTAM Symposium on Laminar-Turbulent Transition, R. Eppler and H. Fasel, editors*, Springer-Verlag, Berlin, pp. 186-190, 1980.

[66] J. F. Mckenzie and K. O. Westphal. Interaction of linear waves with oblique shock waves. *The Physics of Fluids*, 11(11):2350–2362, November 1968.

[67] X. Zhong. Direct Numerical Simulation of Hypersonic Boundary-Layer Transition Over Blunt Leading Edges, Part II: Receptivity to Sound . *AIAA paper 97-0756, 35th AIAA Aerospace Sciences Meeting and Exhibit, January 6-9, Reno, Nevada*, 1997.

[68] H. Hornung. Experimental simulation of high-enthalpy real-gas effects. In J. A. Desideri, R. Glowinski, and J. Periaux, editors, *Hypersonic Flows for Reentry Problems, Volume 1.* Springer-Verlag, 1991.

Thermal Properties			Coefficients for Viscosity Model		
Species	$\theta_v(K)$	$h°(J/kg)$	A_i	B_i	C_i
N_2	3390	0	0.5673×10^{-6}	0.7310	-0.1510×10^{2}
O_2	2270	0	0.2000×10^{-5}	0.6980	-0.1476×10^{2}
NO	2740	2.996×10^{6}	0.1491×10^{-6}	0.7180	-0.1496×10^{2}
N	-	3.3662×10^{7}	0.3171×10^{-1}	0.3475	-0.1391×10^{2}
O	-	1.543×10^{7}	0.1374×10^{-1}	0.5139	-0.1374×10^{2}

Table 1: Thermal properties and coefficients for viscosity model for five species air.

Reaction Rate Coefficients: $k = CT_x^{-\eta} exp(-\theta_d/T_x)$						
Reaction	M_i	k	$C(m^3/kmol \cdot s)$	η	$\theta_d(K)$	T_x
$N_2 + M_i \rightarrow N + N + M_i$	N_2	k_{f11}	4.80×10^{14}	0.5	113000	$\sqrt{T_v T_t}$
	O_2	k_{f12}	1.92×10^{14}	0.5	113000	$\sqrt{T_v T_t}$
	NO	k_{f13}	1.92×10^{14}	0.5	113000	$\sqrt{T_v T_t}$
	N	k_{f14}	4.16×10^{19}	1.5	113000	$\sqrt{T_v T_t}$
	O	k_{f15}	1.92×10^{14}	0.5	113000	$\sqrt{T_v T_t}$
$O_2 + M_i \rightarrow O + O + M_i$	N_2	k_{f21}	7.21×10^{15}	1.0	59500	$\sqrt{T_v T_t}$
	O_2	k_{f22}	3.25×10^{16}	1.0	59500	$\sqrt{T_v T_t}$
	NO	k_{f23}	3.61×10^{15}	1.0	59500	$\sqrt{T_v T_t}$
	N	k_{f24}	3.61×10^{15}	1.0	59500	$\sqrt{T_v T_t}$
	O	k_{f25}	9.02×10^{16}	1.0	59500	$\sqrt{T_v T_t}$
$NO + M_i \rightarrow N + O + M_i$	N_2	k_{f31}	3.97×10^{17}	1.5	75500	$\sqrt{T_v T_t}$
	O_2	k_{f32}	3.97×10^{17}	1.5	75500	$\sqrt{T_v T_t}$
	NO	k_{f33}	7.94×10^{18}	1.5	75500	$\sqrt{T_v T_t}$
	N	k_{f34}	7.94×10^{18}	1.5	75500	$\sqrt{T_v T_t}$
	O	k_{f35}	7.94×10^{18}	1.5	75500	$\sqrt{T_v T_t}$
$N_2 + O \rightarrow NO + N$	-	k_{f4}	6.74×10^{10}	0	38000	$\sqrt{T_v T_t}$
$NO + O \rightarrow O_2 + N$	-	k_{f5}	3.18×10^{6}	1.0	19700	$\sqrt{T_v T_t}$

Table 2: Forward reaction rate coefficients for the Dunn-Kang reacting air model.

Reaction Rate Coefficients: $k = CT_x^{-\eta} exp(-\theta_d/T_x)$						
Reaction	M_i	k	$C(m^3/kmol \cdot s)$	η	$\theta_d(K)$	T_x
$N + N + M_i \rightarrow N_2 + M_i$	N_2	k_{b11}	2.72×10^{10}	0.5	0	T_t
	O_2	k_{b12}	1.10×10^{10}	0.5	0	T_t
	NO	k_{b13}	1.10×10^{10}	0.5	0	T_t
	N	k_{b14}	2.27×10^{15}	1.5	0	T_t
	O	k_{b15}	1.10×10^{10}	0.5	0	T_t
$O + O + M_i \rightarrow O_2 + M_i$	N_2	k_{b21}	6.00×10^{9}	0.5	0	T_t
	O_2	k_{b22}	2.70×10^{10}	0.5	0	T_t
	NO	k_{b23}	3.00×10^{9}	0.5	0	T_t
	N	k_{b24}	3.00×10^{9}	0.5	0	T_t
	O	k_{b25}	7.50×10^{10}	0.5	0	T_t
$N + O + M_i \rightarrow NO + M_i$	N_2	k_{b31}	1.00×10^{14}	1.5	0	T_t
	O_2	k_{b32}	1.00×10^{14}	1.5	0	T_t
	NO	k_{b33}	2.00×10^{15}	1.5	0	T_t
	N	k_{b34}	2.00×10^{15}	1.5	0	T_t
	O	k_{b35}	2.00×10^{15}	1.5	0	T_t
$NO + N \rightarrow N_2 + O$	-	k_{b4}	1.56×10^{10}	0	0	-
$O_2 + N \rightarrow NO + O$	-	k_{b5}	1.30×10^{7}	1.0	3580	$\sqrt{T_v T_t}$

Table 3: Backward reaction rate coefficients for the Dunn-Kang reacting air model.

Reaction Rate Coefficients: $k = CT_x^{-\eta} exp(-\theta_d/T_x)$						
Reaction	M_i	k	$C(m^3/kmol \cdot s)$	η	$\theta_d(K)$	T_x
$N_2 + M_i \rightarrow N + N + M_i$	N_2	k_{f11}	7.00×10^{18}	1.6	113200	$\sqrt{T_v T_t}$
	O_2	k_{f12}	7.00×10^{18}	1.6	113200	$\sqrt{T_v T_t}$
	NO	k_{f13}	7.00×10^{18}	1.6	113200	$\sqrt{T_v T_t}$
	N	k_{f14}	3.00×10^{19}	1.6	113200	$\sqrt{T_v T_t}$
	O	k_{f15}	3.00×10^{19}	1.6	113200	$\sqrt{T_v T_t}$
$O_2 + M_i \rightarrow O + O + M_i$	N_2	k_{f21}	2.00×10^{18}	1.5	59500	$\sqrt{T_v T_t}$
	O_2	k_{f22}	2.00×10^{18}	1.5	59500	$\sqrt{T_v T_t}$
	NO	k_{f23}	2.00×10^{18}	1.5	59500	$\sqrt{T_v T_t}$
	N	k_{f24}	1.00×10^{19}	1.5	59500	$\sqrt{T_v T_t}$
	O	k_{f25}	1.00×10^{19}	1.5	59500	$\sqrt{T_v T_t}$
$NO + M_i \rightarrow N + O + M_i$	N_2	k_{f31}	5.00×10^{12}	0	75500	$\sqrt{T_v T_t}$
	O_2	k_{f32}	5.00×10^{12}	0	75500	$\sqrt{T_v T_t}$
	NO	k_{f33}	1.10×10^{14}	0	75500	$\sqrt{T_v T_t}$
	N	k_{f34}	1.10×10^{14}	0	75500	$\sqrt{T_v T_t}$
	O	k_{f35}	1.10×10^{14}	0	75500	$\sqrt{T_v T_t}$
$N_2 + O \rightarrow NO + N$	-	k_{f4}	6.40×10^{14}	1.0	38400	T_t
$NO + O \rightarrow O_2 + N$	-	k_{f5}	8.40×10^{9}	0	19450	T_t

Table 4: Forward reaction rate coefficients for the Park reacting air model.

Equilibrium Constant Data for Park Model $K^i_{eq} = \exp\left(A^i_1(\frac{T}{10000}) + A^i_2 + A^i_3 \ln(\frac{10000}{T}) - A^i_4(\frac{10000}{T}) + A^i_5(\frac{10000}{T})^2\right)$					
Reaction	A^i_1	A^i_2	A^i_3	A^i_4	A^i_5
$N_2 \rightleftharpoons N + N$	1.476600	1.62910	1.21530	11.45700	−0.009444
$O_2 \rightleftharpoons O + O$	0.509890	2.47730	1.71320	6.54410	0.29591
$NO \rightleftharpoons N + O$	0.507650	0.73575	0.48042	7.49790	−0.16247
$N_2 + O \rightleftharpoons NO + N$	0.969210	0.89329	0.73531	3.95960	0.006818
$NO + O \rightleftharpoons O_2 + N$	−0.002428	−1.74150	−1.23310	0.95365	−0.045850

Table 5: Equilibrium constants for the Park reacting air model.

Cases	$Q_{NS}(W/m^2)$	$Q_{BL}(W/m^2)$	$Diff$
Hornung (Park)	0.7408×10^7	0.8504×10^7	14.8%
Hornung (D-K)	0.9638×10^7	0.9951×10^7	3.2%
Sanderson-B (Park)	0.7030×10^7	0.7868×10^7	11.9%
Sanderson-B (D-K)	0.9960×10^7	0.9878×10^7	−0.8%
Sanderson-C1 (D-K)	0.1806×10^8	0.1907×10^8	5.6%
Sanderson-C2 (D-K)	0.1211×10^7	0.1175×10^7	−3.0%

Table 6: Comparison of Heat flux at stagnation point compuated by NS-Equ. and BL-Equ. $Diff = (Q_{NS} - Q_{BL})/Q_{NS}$

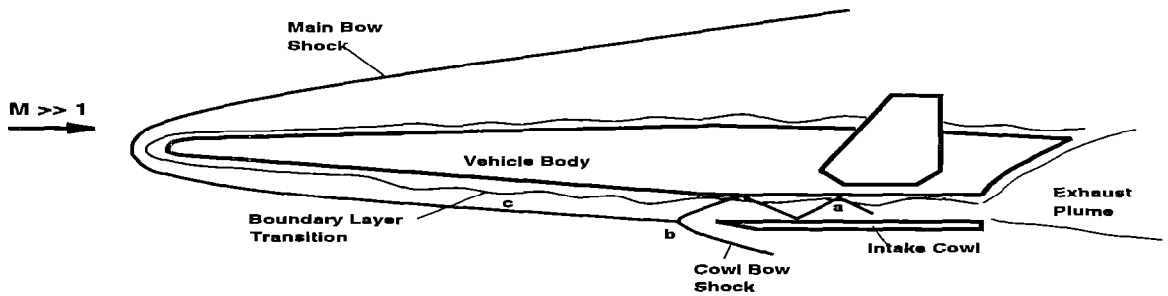

Figure 1: A schematic of a generic hypersonic lifting vehicle with boundary-layer transition.

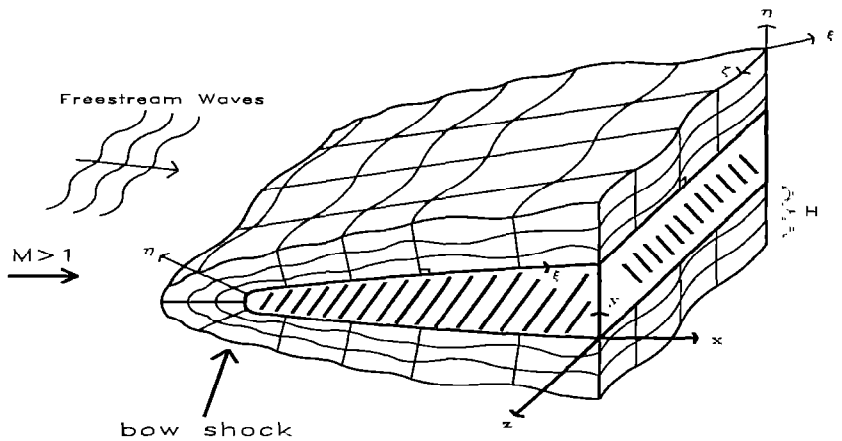

Figure 2: A schematic of 3-D shock fitted grids for the direct numerical simulation of hypersonic boundary-layer receptivity to freestream disturbances over a blunt leading edge.

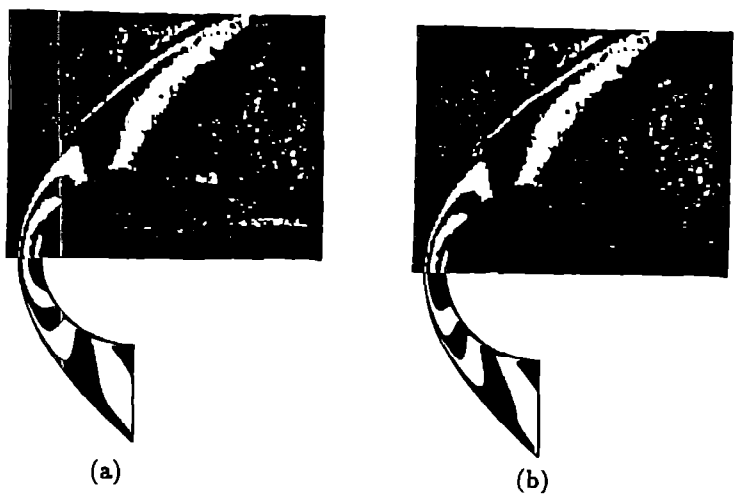

Figure 3: Comparison of current pressure contours (bottom) with experimental results of Hornung (Ref. [68]) (top). (a)Park model, (b) Dunn-Kang model.

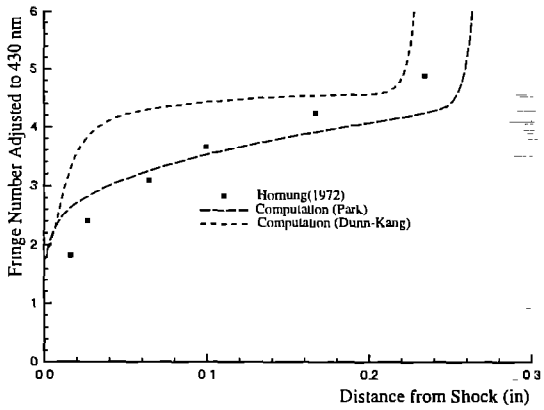

Figure 4: Computed fringe numbers for the two chemistry models compared with experimental values of Hornung (Ref. [36])along the stagnation line.

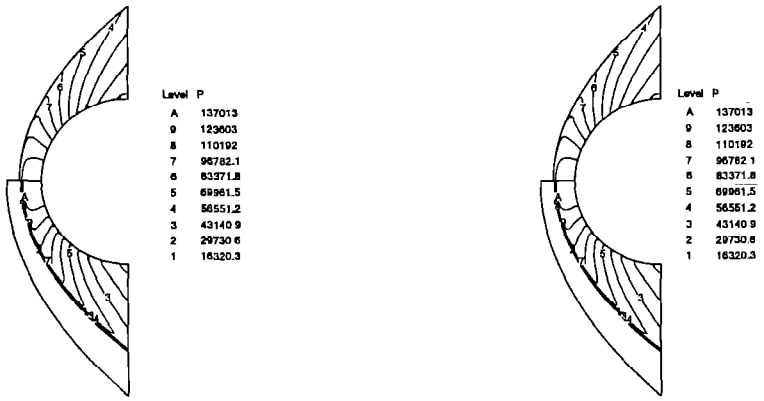

(a) (b)

Figure 5: Comparison of current pressure contours (top) with Furumoto's computational results(bottom). (a)Park model, (b) Dunn-Kang model.

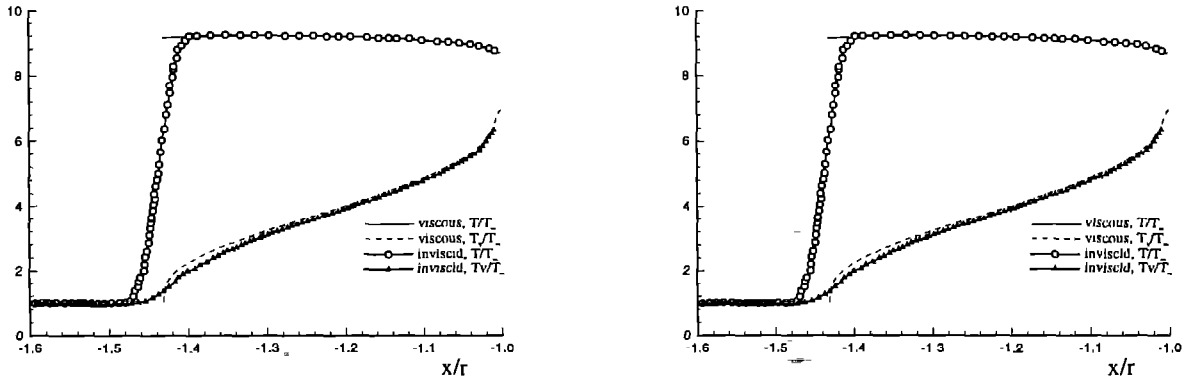

Figure 6: Comparison of temperature profile along the stagnation line between viscous flow and inviscid flow, left:$P_\infty = 50Pa$; right: $P_\infty = 500Pa$.

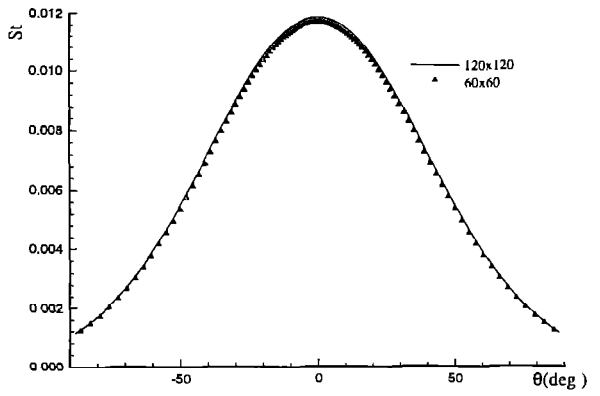

Figure 7: Computed surface Stanton number ($St = \frac{q_w}{\rho_\infty u_\infty h_{0\infty}}$) profiles.

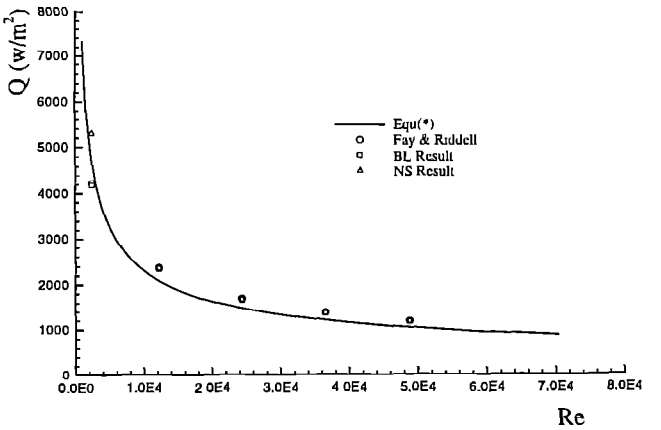

Figure 10: Heat flux at stagnation point. * Equ. 65

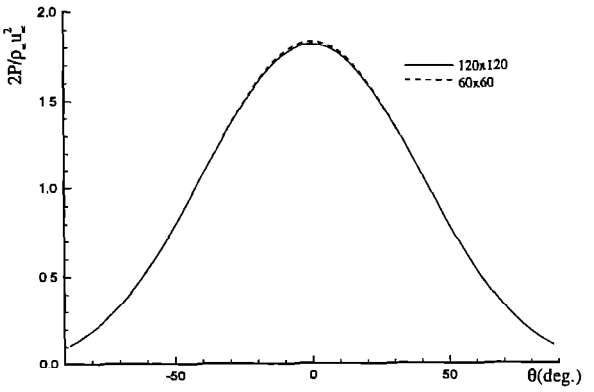

Figure 8: Normalized pressure ($\frac{2P_w}{\rho_\infty u_\infty^2}$) profile along the surface.

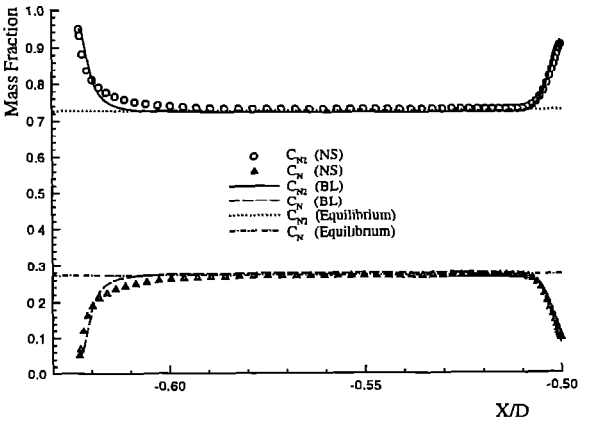

Figure 11: Profile of Mass fraction along the stagnation line.

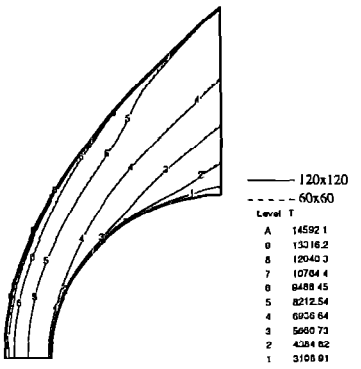

Figure 9: Computed cotours of translational temperature.

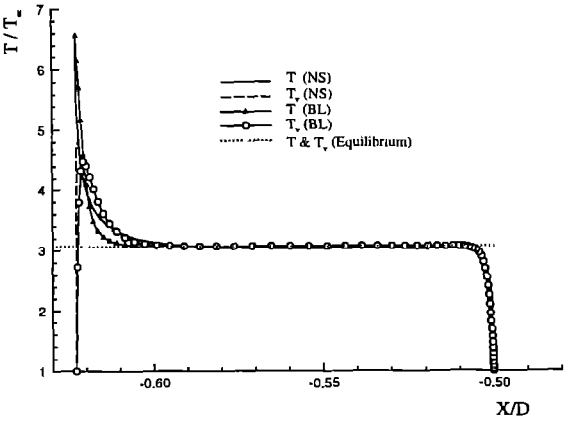

Figure 12: Profile of temperature along the stagnation line.

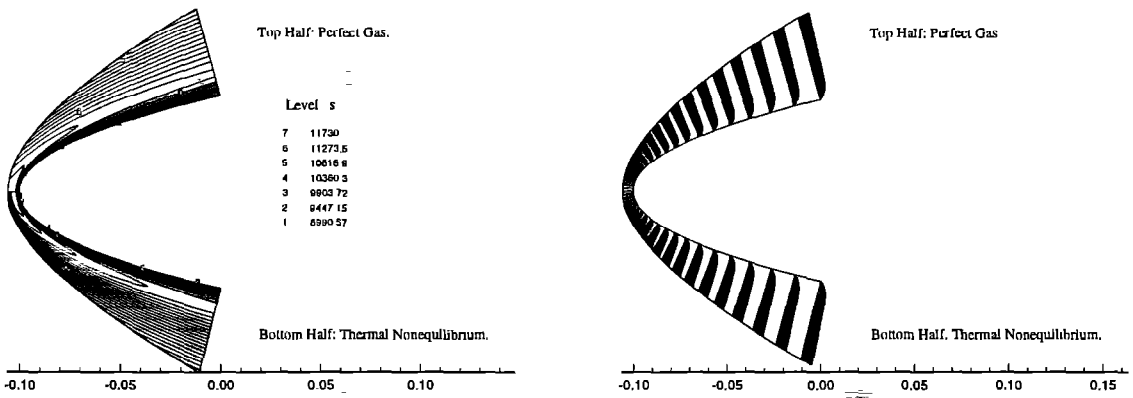

Figure 13: Base flow solutions compared with that of perfect gas, left figure: entropy contours, right figure: velocity vectors.

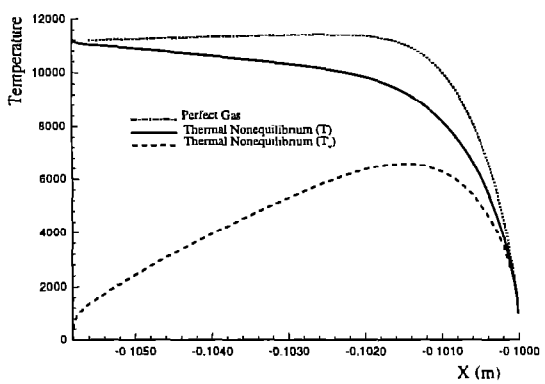

Figure 14: Profile of temperature along the stagnation line.

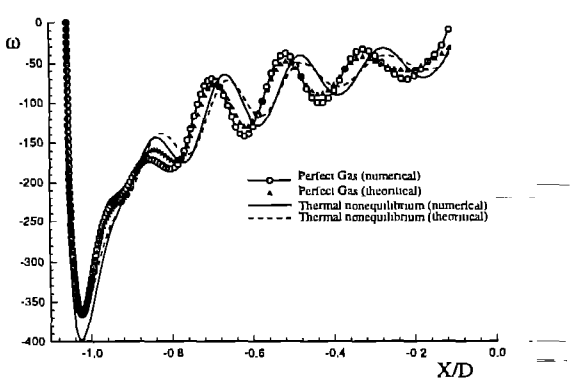

Figure 15: Comparison of vorticity jump across the bowl shock.

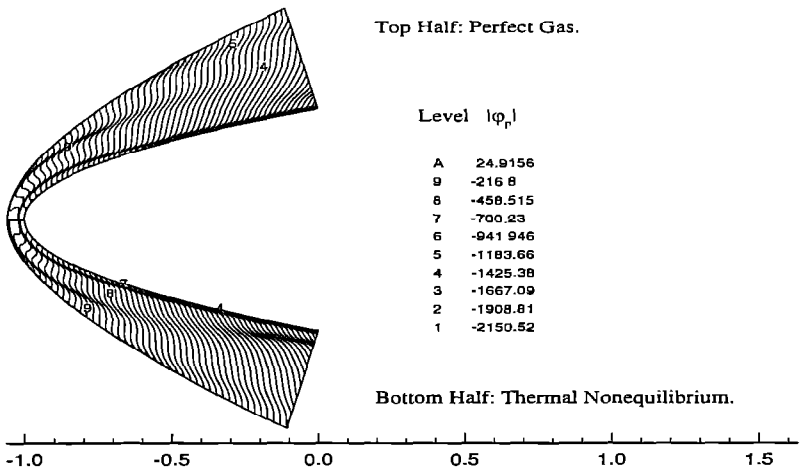

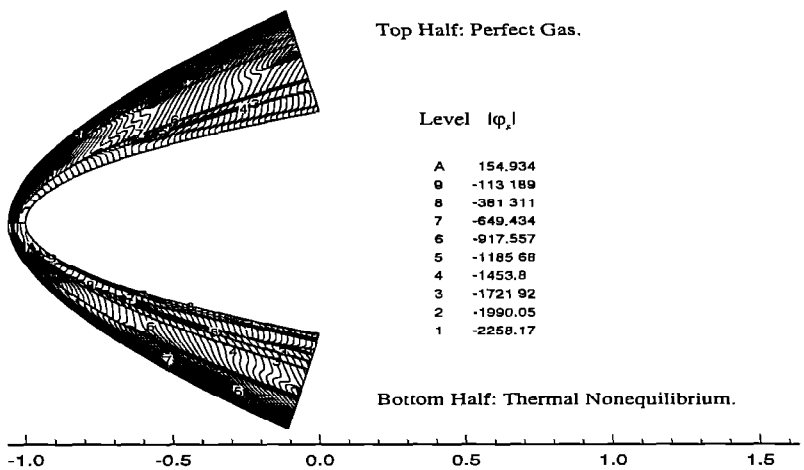

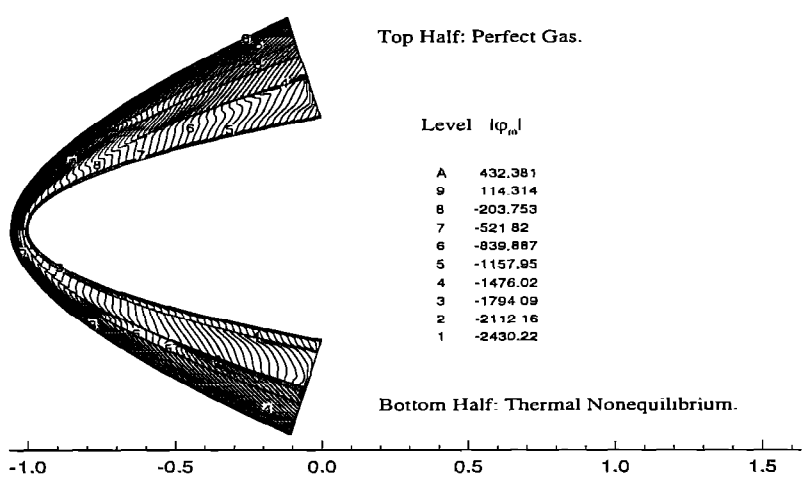

Figure 16: Fourier phase angle of pressure, entropy and vorticity perturbation.

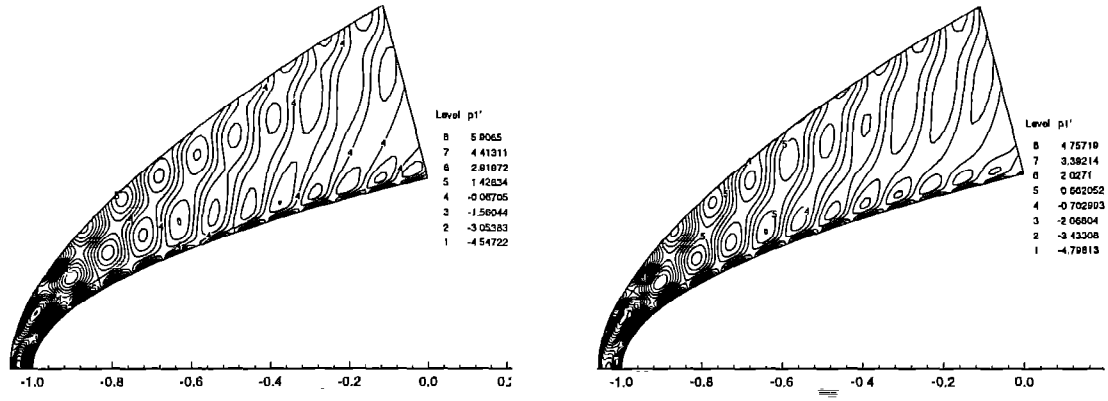

Figure 17: Comparison of instantaneous contours of perturbations of pressure between perfect gas flow (left figure) and thermally nonequilibrium flow (right figure).

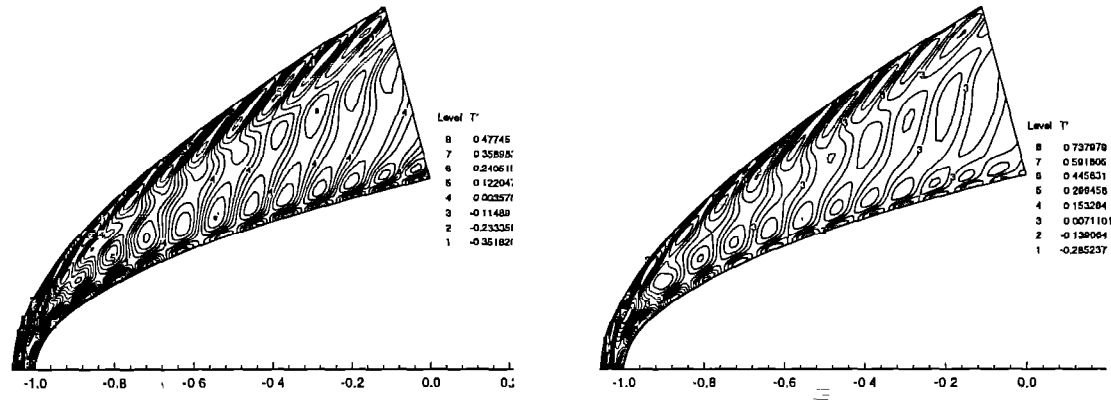

Figure 18: Comparison of instantaneous contours of perturbations of temperature between perfect gas flow (left figure) and thermally nonequilibrium flow (right figure).

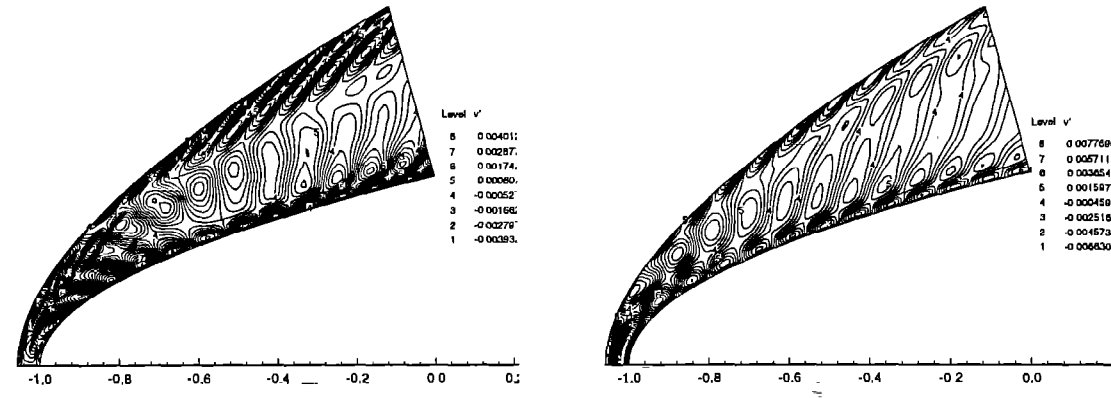

Figure 19: Comparison of instantaneous contours of perturbations of vertical velocity between perfect gas flow (left figure) and thermally nonequilibrium flow (right figure).

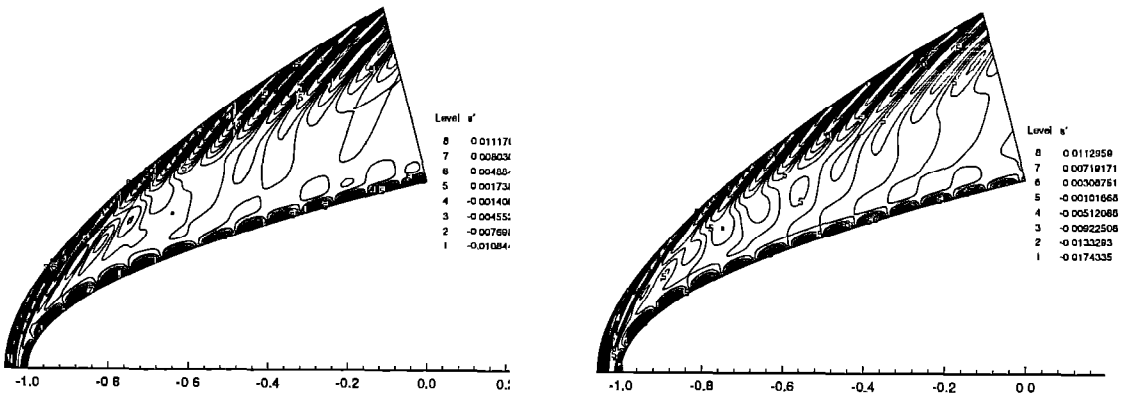

Figure 20: Comparison of instantaneous contours of perturbations of entropy between perfect gas flow (left figure) and thermally nonequilibrium flow (right figure).

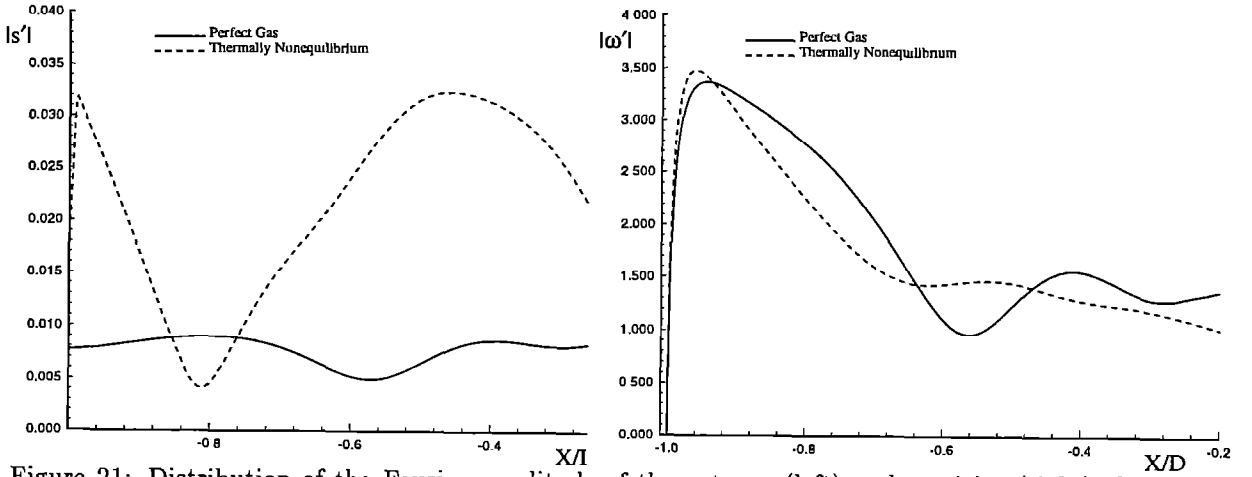

Figure 21: Distribution of the Fourier amplitude of the entropy (left) and vorticity (right) along the parabola surface.

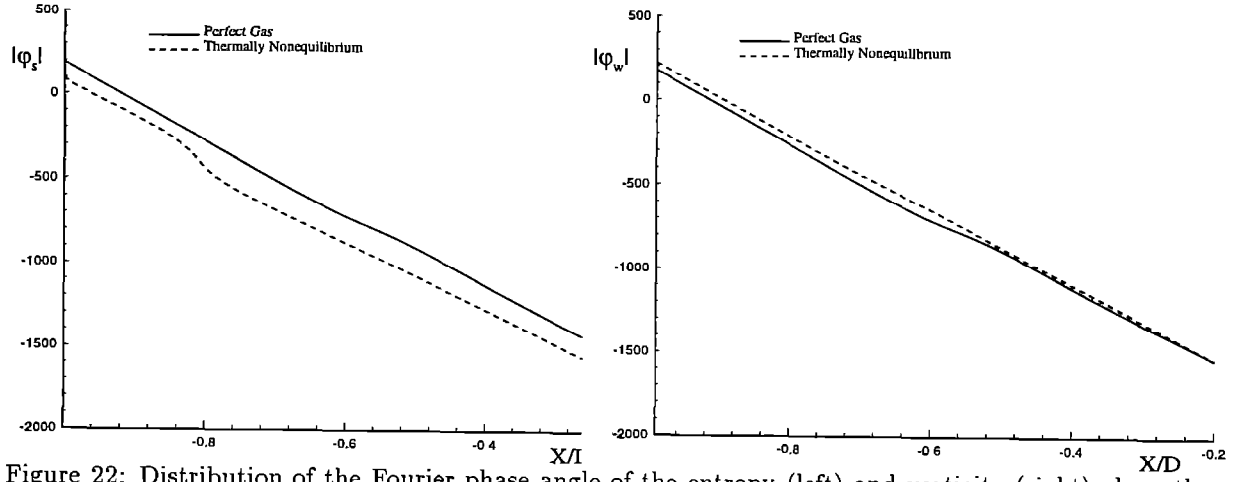

Figure 22: Distribution of the Fourier phase angle of the entropy (left) and vorticity (right) along the parabola surface.

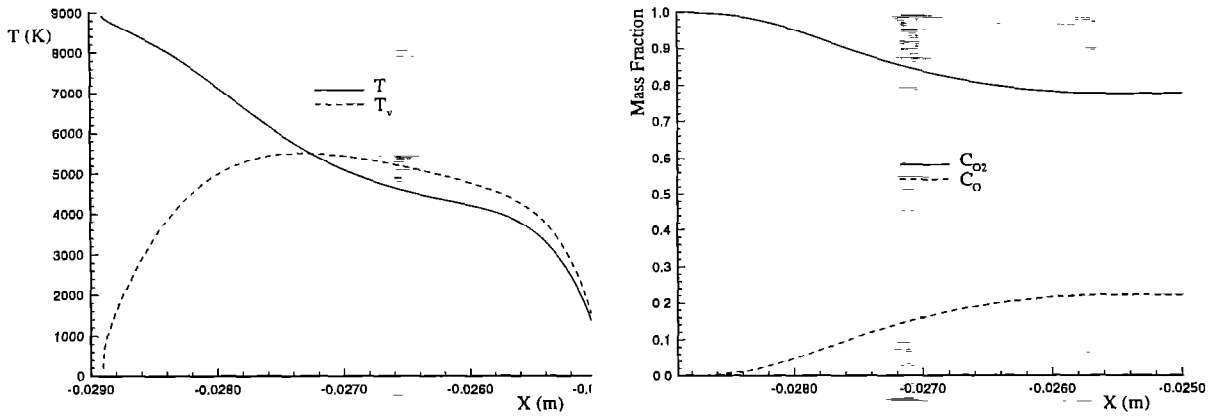

Figure 23: Profile of temperature and mass fraction along the stagnation line.

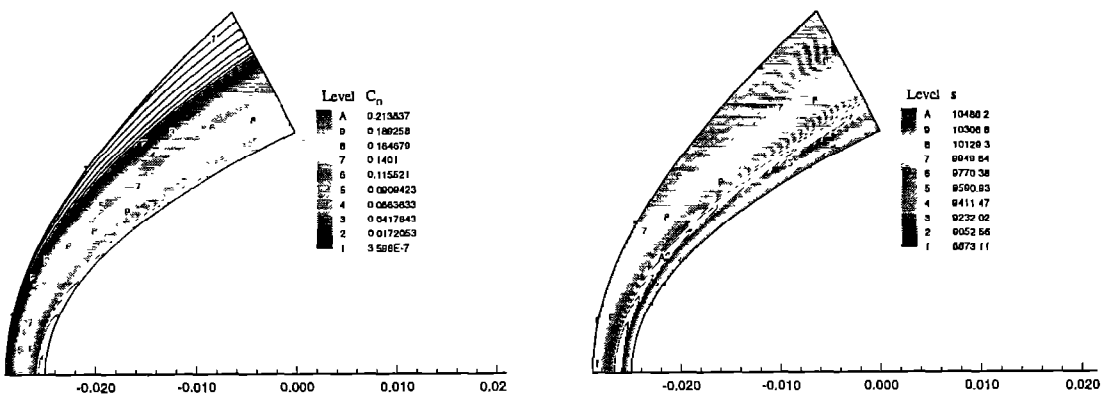

Figure 24: Base flow solution of atomic oxygen fraction and entropy contours.

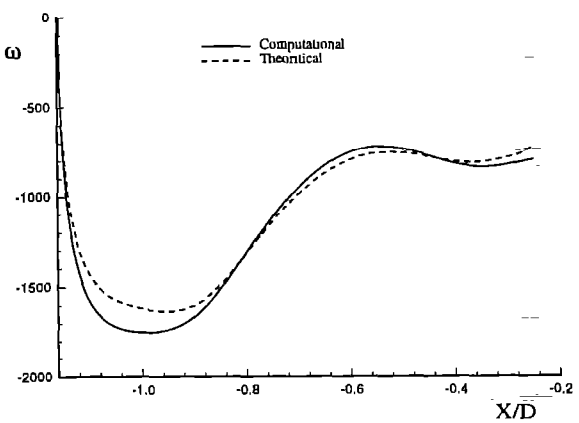

Figure 25: Vorticity jump across the unsteady bowl shock.

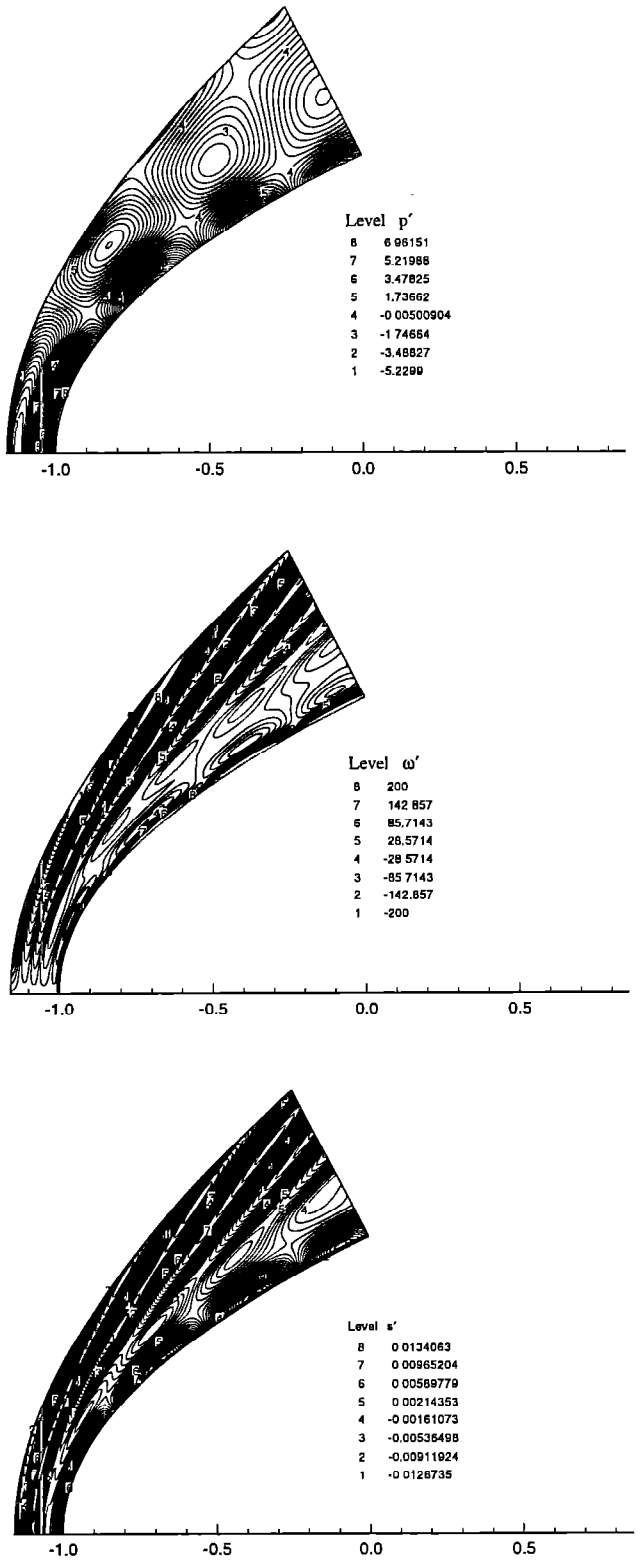

Figure 26: Instantaneous perturbation of pressure, vorticity and entropy.